

# Stellar Disks in Aquarius Dark Matter Haloes

Jackson DeBuhr<sup>1</sup>, Chung-Pei Ma<sup>1</sup>, Simon D. M. White<sup>2</sup>

<sup>1</sup>*Department of Astronomy, University of California, Berkeley, CA 94720, USA*

<sup>2</sup>*Max-Planck-Institut für Astrophysik, Karl-Schwarzschild-Str. 1, 85748 Garching, Germany*

26 March 2022

## ABSTRACT

We investigate the gravitational interactions between live stellar disks and their dark matter halos, using  $\Lambda$ CDM haloes similar in mass to that of the Milky Way taken from the Aquarius Project. We introduce the stellar disks by first allowing the haloes to respond to the influence of a growing rigid disk potential from  $z = 1.3$  to  $z = 1.0$ . The rigid potential is then replaced with star particles which evolve self-consistently with the dark matter particles until  $z = 0.0$ . Regardless of the initial orientation of the disk, the inner parts of the haloes contract and change from prolate to oblate as the disk grows to its full size. When the disk normal is initially aligned with the major axis of the halo at  $z = 1.3$ , the length of the major axis contracts and becomes the minor axis by  $z = 1.0$ . Six out of the eight disks in our main set of simulations form bars, and five of the six bars experience a buckling instability that results in a sudden jump in the vertical stellar velocity dispersion and an accompanying drop in the  $m = 2$  Fourier amplitude of the disk surface density. The bars are not destroyed by the buckling but continue to grow until the present day. Bars are largely absent when the disk mass is reduced by a factor of two or more; the relative disk-to-halo mass is therefore a primary factor in bar formation and evolution. A subset of the disks is warped at the outskirts and contains prominent non-coplanar material with a ring-like structure. Many disks reorient by large angles between  $z = 1$  and  $z = 0$ , following a coherent reorientation of their inner haloes. Larger reorientations produce more strongly warped disks, suggesting a tight link between the two phenomena. The origins of bars and warps appear independent: some disks with strong bars show little disturbances at the outskirts, while the disks with the weakest bars show severe warps.

**Key words:** dark matter - galaxies:formation - galaxies:evolution - galaxies:kinematics and dynamics - galaxies:structure - cosmology:theory

## 1 INTRODUCTION

At low redshift stellar disks are ubiquitous in galaxies of similar mass to the Milky Way. The properties of these disks show many regularities (see the review by van der Kruit & Freeman 2011 and references therein), but reproducing these regularities in simulations of galaxy formation in a  $\Lambda$ CDM universe has been a major challenge, although recent improvements in subgrid physics and numerical resolution have begun to result in disks that resemble those seen in dwarf galaxies and the Milky Way (e.g., Governato et al. 2010; Agertz et al. 2011; Guedes et al. 2011). Each disk is simulated under a specific schematic representation of the feedback physics, and at considerable computational costs.

Results from the Aquila comparison project (Scannapieco et al. 2012), however, suggest that the latest hydrodynamic simulations can not yet uniquely predict the properties of baryons in a galaxy, even when the assembly history of its host halo is fully specified. When a common dark matter

halo is resimulated with gas with nine cosmological hydrodynamic codes, large code-to-code differences are found in the  $z = 0$  stellar mass, size, morphology, and gas content. The variations are mainly due to the different implementations of feedback. The feedback models that are more effective at suppressing the baryonic mass in the galaxy are better at matching the observed scaling relations of the global properties of the galaxies, but they do not necessarily produce more realistic disks.

The goal of this paper is to investigate the gravitational interactions between live stellar disks and their dark matter haloes, when these are themselves evolving in their full cosmological context. Rather than focusing on how to form a disk with realistic structure, we choose to study how preformed stellar disks are influenced by the cosmologically driven evolution of the haloes in which they are embedded. We use haloes from the Aquarius Project (Springel et al. 2008) because they provide a particularly well studied set of high resolution haloes of similar mass.

We simulate each disk-halo system in two phases, first by allowing each Aquarius dark matter halo to respond adiabatically to a growing rigid disk potential between  $z = 1.3$  and  $1.0$ , and then by inserting a live disk of stellar particles that are evolved with the dark matter particles from  $z = 1.0$  to today. We insert disks in four Aquarius haloes (A, B, C, and D), with the disk normal initially aligned with the minor or major axis of the inner halo as measured at  $z = 1.3$ . The main results in this paper are drawn from these eight simulations; several additional runs are also performed to test numerical convergences and to assess the impact of different disk models.

Our study complements several earlier papers that used the Aquarius haloes for numerical explorations of the formation and evolution of galaxies like our own. Scannapieco et al. (2009) resimulated a number of the original Aquarius haloes including the effects of a realistic multi-phase, star-forming gas. Disks were found to form at  $z \gtrsim 2$ , but were often destroyed again by mergers or instabilities, depending on the particular assembly history of each object. Tissera et al. (2010) analyzed the effects of the baryons on the dark matter halos in the same set of simulations. They found the response of the haloes to baryon condensation to depend on the specifics of how the halo was constructed. Cooper et al. (2010) tagged subsets of dark matter particles in the Aquarius haloes with stellar populations assigned according to a semi-analytic model of galaxy formation and studied the spatial and kinematic properties of the stellar haloes. Aumer & White (2012) investigated properties of stellar disks which they formed in the Aquarius haloes by allowing a smooth, spherically symmetric cloud of rotating gas to cool and condense at halo center.

Numerous earlier studies have inserted live stellar disks into dark matter haloes, most of them with an idealized setup and/or environment for the disks and haloes. Some  $N$ -body studies focused on isolated disk and halo systems and studied internal or secular evolution, e.g., Dubinski (1994); Athanassoula (2002); Debattista et al. (2006); Berentzen & Shlosman (2006); Machado & Athanassoula (2010). Other studies presented results for the effects of external perturbations such as infalling satellites on an existing live disk in a halo, e.g., Quinn & Goodman (1986); Mihos et al. (1995); Walker et al. (1996); Sellwood et al. (1998); Velazquez & White (1999); Font et al. (2001); Benson et al. (2004); Gauthier et al. (2006); Curir et al. (2006, 2007); Bournaud et al. (2007); Hopkins et al. (2008); Read et al. (2008); Kazantzidis et al. (2008, 2009); Purcell et al. (2009); Chakrabarti & Blitz (2009); Moster et al. (2012). Our study takes advantage of some of the most realistic and well resolved dark matter haloes currently available. This setup allows us to investigate the full dynamical interactions of live stellar disks and live haloes in the presence of cosmological mergers and large-scale tidal fields, without having to make assumptions about the triaxiality and equilibrium state of the halo, or about the orbits and masses of the infalling satellites.

The organization of this paper is as follows. Section 2 describes the methodology used to insert the stellar disk into the halo and the parameters used in the simulations. The effects of the growing rigid disk on the axial lengths and triaxiality of the haloes between  $z = 1.3$  and  $1.0$  are described in Section 3. Results for the evolution of the live stellar disks in our main set of simulations are presented in Section 4.

Here we investigate the radial and vertical structures of the disks (Sec. 4.1), the formation and evolution of stellar bars (Sec. 4.2), the velocity profiles and heating due to the bars and other transient features in the disk (Sec. 4.3), and the warps in the outskirts of the disks and the correlation of the warps with the large-scale rotation of the haloes (Sec. 4.4). Results from alternative disk models such as disks with lowered stellar masses and disks with non-cooling gas are given in Section 5.

## 2 METHODS AND SIMULATION PARAMETERS

To study the evolution of stellar disks in a full cosmological context, we begin with a suite of dark matter haloes from the Aquarius simulations (Springel et al. 2008). We then add a stellar disk to each Aquarius halo in two phases. During the first phase – starting at  $z = 1.3$  and ending at  $z = 1.0$  – the dark matter is allowed to react to a rigid disk potential whose mass increases from zero at  $z = 1.3$  to the desired final mass at  $z = 1.0$ . At the start of the second ‘live’ phase at  $z = 1.0$ , the rigid disk is replaced with live simulation particles. This live disk is then evolved self-consistently along with all the dark matter particles to  $z = 0$ . Below we describe each step in detail.

### 2.1 Dark Matter Haloes

The high-resolution zoom-in simulations of dark matter haloes in the Aquarius Project are chosen from a lower resolution version of the Millennium-II Simulation (Boylan-Kolchin et al. 2009). These resimulated haloes are chosen randomly from those with a mass similar to that of the Milky Way, and which does not have a massive close neighbor at  $z = 0$ . These haloes are therefore good candidates to host Milky Way-like disk galaxies. The cosmological model is  $\Lambda$ CDM with  $\Omega_\Lambda = 0.75$ ,  $\Omega_m = 0.25$ ,  $\Omega_b = 0.04$ ,  $\sigma_8 = 0.9$  and  $H_0 = 73 \text{ km s}^{-1} \text{ Mpc}^{-1}$ .

In this work we select haloes A, B, C and D at resolution level 5. This resolution level corresponds to dark matter particle masses of  $\approx 3 \times 10^6 M_\odot$ , and a comoving gravitational force softening length of 685 pc. The virial mass (defined using an overdensity of  $200\rho_{crit}$ ) of the four dark matter haloes at  $z = 0$  is  $1.49 \times 10^{12} M_\odot$ ,  $7.11 \times 10^{11} M_\odot$ ,  $1.61 \times 10^{12} M_\odot$ , and  $1.49 \times 10^{12} M_\odot$  for A, B, C and D, respectively. Despite their comparable final masses, the four haloes have different merger histories. While each halo has accreted a fair number of small subhaloes during the course of the simulation, the level of activity for infalling satellites above one tenth the disk mass  $M_d$  (chosen to be  $M_d = 5 \times 10^{10} M_\odot$  for our fiducial disk model) varies from halo to halo. Haloes A and B are relatively quiet after  $z \sim 0.7$  when a subhalo of mass  $\sim 0.3M_d$  impacts in each. Halo C has a number of larger subhaloes in the latter part of the simulation ( $z < 0.5$ ), where the two most massive subhaloes have masses of  $0.22M_d$  and  $0.16M_d$ . Halo D has the most active history, with appreciable encounters spread throughout the simulation. Although these impacts are defined at the halo level, and thus are not necessarily close enough to the disk to have a dynamical effect, they are candidates for study in future work linking specific halo substructures to features of the disk evolution.

Run Name	Halo	Disk Orientation	$M_d$ [ $10^{10}M_\odot$ ]	$R_d$ [kpc]	$z_d$ [kpc]	$Q_{bar}$ [ $z = 1.0$ ]	Notes
AMinor	A5	Minor	5.00	3.00	0.60	0.98	
AMajor	A5	Major	5.00	3.00	0.60	0.99	
AMinorHalf	A5	Minor	2.50	2.38	0.48	1.13	
AMinorThird	A5	Minor	1.67	2.08	0.42	1.23	
AMinorGas	A5	Minor	5.00	3.00	0.60	-	initial gas fraction of 0.4
AMinorHR	A5	Minor	5.00	3.00	0.60	0.98	$5 \times 10^5$ particles in disk
AMinor09	A5	Minor	5.00	3.00	0.60	1.00	Transition to live disk at $z = 0.9$
ANoDisk	A5	-	-	-	-	-	No disk
BMinor	B5	Minor	5.00	3.00	0.60	0.83	
BMajor	B5	Major	5.00	3.00	0.60	0.81	
BNoDisk	B5	-	-	-	-	-	No disk
CMinor	C5	Minor	5.00	3.00	0.60	1.03	
CMajor	C5	Major	5.00	3.00	0.60	1.03	
CMinorHalf	C5	Minor	2.50	2.38	0.48	1.15	
CMinorThird	C5	Minor	1.67	2.08	0.42	1.26	
CMinorGas	C5	Minor	5.00	3.00	0.60	-	initial gas fraction of 0.4
CNoDisk	C5	-	-	-	-	-	No disk
DMinor	D5	Minor	5.00	3.00	0.60	0.93	
DMajor	D5	Major	5.00	3.00	0.60	0.92	
DNoDisk	D5	-	-	-	-	-	No disk

**Table 1.** Simulation Parameters: “Halo” refers to the Aquarius dark matter halo (and resolution level) used in the simulation. “Disk Orientation” indicated whether disk normal is initially aligned with the major or with the minor axis of the halo at  $z = 1.3$ . Parameters  $M_d$ ,  $R_d$ , and  $z_d$  are the total mass, scale length, and scale height of the disk at the start of the live phase at  $z = 1.0$ , respectively. The bar criterion parameter  $Q_{bar}$  is measured at  $z = 1.0$ ; it is defined in eq. (5) and  $Q_{bar} > 1.1$  indicates stability against bar formation.

## 2.2 Phase 1: Adding a Rigid Disk

We modified a version of GADGET-2 (Springel 2005) to add a rigid stellar disk potential to the existing dark matter particles. The potential corresponds to an exponential disk with density:

$$\rho(R, z, t) = \frac{M_d(t)}{4\pi R_d^2 z_d} e^{-R/R_d} \operatorname{sech}^2\left(\frac{z}{z_d}\right), \quad (1)$$

where  $R_d$  and  $z_d$  are the scale length and scale height of the disk, respectively, and  $M_d(t)$  is the mass of the disk at time  $t$ . The mass of the disk is increased linearly in the scale factor, which is approximately linear in time, from zero at  $z = 1.3$  to the total mass,  $M_d$ , at  $z = 1.0$ .

The center of the disk is initially placed at the minimum of the gravitational potential of the main Aquarius halo at  $z = 1.3$ . The initial velocity of the disk is set to the velocity of the potential minimum. To orient the disk, we first determine the principal axes of the gravitational potential of the dark matter halo by constructing equipotential surfaces of the dark matter particles and fitting ellipsoids to them. The disk normal is chosen to be aligned with either the minor or major axis of the halo at  $z = 1.3$ . We refer to these two disk orientations as “Minor” and “Major” in the rest of the paper.

During this phase of the simulation, each dark matter particle feels a force from this rigid potential in addition to the normal gravitational interactions with all the dark matter particles. These extra forces are applied in a self-consistent manner, with the disk center experiencing the third-law force pairs from each dark matter particle. This procedure assures that linear momentum is conserved and the disk center moves with the center of the main halo.

The orientation of the rigid potential is fixed during this phase. This choice appears appropriate since the dark matter haloes do not rotate much between  $z = 1.3$  and 1.0. We do find, however, that the principal axes of the haloes can drift by up to 20 degrees between  $z = 1.3$  and 1.0. This drift implies that if our disk’s normal is initially aligned with one of the halo’s axes at  $z = 1.3$ , it may become slightly misaligned by  $z = 1.0$ . We have performed a test run in which the live disk’s normal is exactly aligned with the minor axis of halo A at  $z = 1.0$  (rather than at  $z = 1.3$  as in the fiducial runs). We find this slight adjustment in the initial alignment to make little difference in the subsequent evolution of the disk.

## 2.3 Phase 2: Live Disk

Phase 1 above allows the dark matter particles to respond adiabatically to the presence of a growing rigid disk potential between  $z = 1.3$  and 1.0. Phase 2 begins at  $z = 1.0$  when we add live disk particles to the simulations.

The initial conditions of the live disk particles are generated by creating a model of the full potential of the system, and finding an approximate solution to the Jeans equations. The potential of the disk is easily computed from the model density, but for the halo potential we perform a fit to the dark matter particle potentials at the end of phase 1 at  $z = 1.0$  (excluding the contribution to the potential from the rigid disk). The halo particles are projected into coordinates centered on the disk with the  $z$  axis aligned with the disk normal. The potential values of the halo particles are fit to the following functional form:

$$\Phi = v_c^2 \ln \left[ 1 + \frac{u^2}{R_c^2} \right], \quad u^2 = z^2 + \frac{x^2 + y^2}{a_3^2}, \quad (2)$$

where  $u$  is an ellipsoidal coordinate, and  $v_c$ ,  $R_c$  and  $a_3$  are parameters of the fit. This definition of  $u$  forces the description of the background halo potential to have one of its principal axes along the disk normal. This is a good assumption for the evolved halo in both the major and minor orientation. This definition also assumes a potential which is axisymmetric with respect to the disk normal direction.

Once the live disk particles are added at  $z = 1.0$ , the rigid disk potential is turned off and both the stellar and dark matter particles are allowed to evolve self-consistently until  $z = 0$ .

To test the stability of the live disks generated with this method, we have evolved the disk particles in isolation subject to a static background potential equal to the fitted halo potential at  $z = 1.0$  in equation (2). The evolved disk is stable over a long time and develops no significant structure. The strong bar formation in most of the live simulations that we report below must therefore depend on reinforcement by a coherent response of the halo to the growing perturbation.

## 2.4 Disk Parameters

We have run a suite of simulations with a range of disk parameters and properties to assess the robustness of our results. The main parameters of the simulations are summarized in Table 1.

Our fiducial disk model assumes a stellar disk mass of  $M_d = 5 \times 10^{10} M_\odot$ , a scale length of  $R_d = 3$  kpc, and a scale height of  $z_d = 0.6$  kpc. These values are chosen to resemble the Milky Way’s disk today (Jurić et al. 2008; McMillan 2011). This should also be a reasonable choice for  $z = 1.0$  as disk size does not exhibit strong evolution between  $z \sim 1.0$  and 0 (Trujillo et al. 2006). Each realization of the disk uses  $2 \times 10^5$  stellar particles with a comoving gravitational force softening of 137 pc for these particles. For each halo, we run two separate simulations for two disk orientations, in which the initial disk normal is aligned either with the minor or with the major axis of the halo at  $z = 1.3$ .

For a direct comparison between simulations without and with a disk, we run dark-matter-only simulations with the particle positions and velocities from the Aquarius  $z = 1.0$  snapshot as initial conditions until  $z = 0.0$  (labeled with ‘NoDisk’ in Table 1). Although the particle positions and velocities at  $z = 0.0$  are not identical to those in the original Aquarius runs due to differences in machine and numerical details, the properties of the haloes are very similar.

To quantify the dependence of our results on the assumed disk mass, we run additional simulations with one half and one third the fiducial disk mass in the minor orientation in the A and C halos (labeled ‘Half’ and ‘Third’). The scale lengths are reduced in accordance with the observed relation,  $R_d \propto M_d^{1/3}$  (Shen et al. 2003).

Two additional simulations are performed with haloes A and C that include a gaseous component with initial gas fraction of  $f_g = 0.4$ . This component is comprised of  $10^5$  SPH particles. The gas particles are initialized with the same radial profile as the stellar component, but the vertical structure is initialized in hydrostatic equilibrium. For simplicity, the gas used in these runs is not star forming and does not

cool. We include this component to test if a gas component helps stabilize the stars in a disk. A more realistic simulation would turn most of the gas at  $z = 1$  into stars by  $z = 0$ .

To determine the effect of changing the time at which the disk becomes live, we have run a simulation in which the rigid disk potential is transitioned to a live disk at  $z = 0.9$  rather than  $z = 1.0$  (‘AMinor09’ in Table 1). In this run the rigid disk potential grows from zero to its final mass over the period of  $z = 1.3$  and 0.9. Other parameters are identical to those used in the AMinor simulation.

Finally, to assess if our results are converged with respect to the stellar disk particle number, we perform a simulation of the AMinor disk with  $5 \times 10^5$  instead of  $2 \times 10^5$  stellar particles. This run is listed as ‘AMinorHR’ in Table 1.

## 3 EFFECTS OF RIGID STELLAR DISKS ON DARK MATTER HALOES

In this section we discuss the effects of the rigid disk potential on the shapes and orientations of the dark matter haloes during the disk growing phase of the simulations ( $z = 1.3$  to 1.0). By comparing our simulations with the original Aquarius dark-matter-only haloes, we can quantify how the presence of stellar disks in more realistic simulations alters the distributions of the dark matter.

To measure the triaxiality of each halo, we determine the principal axes by constructing equipotential surfaces (excluding the contribution to the potential from the rigid disk) near the center of the halo with the procedure discussed in Sec 2.3. In general, the equipotential surfaces are fit well by ellipsoids, failing to be ellipsoidal only in the presence of significant substructure. In haloes B and D, there are significant subhaloes near the position of the disk initially, so the fit to an ellipsoid fails for a few potential bins. Nevertheless, the fit performs well for most of the potential bins (and hence most radii) and for most times.

Figs. 1 and 2 illustrate the effects of the rigid disk on the triaxiality of the dark matter haloes. Fig. 1 shows the surface density of dark matter particles in the inner 40 kpc of haloes B (top) and D (bottom) at the initial time  $z = 1.3$  (left column), and at  $z = 1.0$  for runs without the disk (middle column) and with the disk (right column). Fig. 2 plots the time evolution of the axial lengths of each halo, where the orientations as well as axial lengths are computed at each snapshot. The left two columns of Fig. 2 show the axial ratios determined from equipotential surfaces at  $\sim 5$  kpc, and the right column shows the evolution of the length of the initial major axis for a chosen equipotential surface. The results are representative of the other equipotential surfaces.

Without stellar disks, Figs. 1 (left two panels) and 2 (dashed curves) show that the inner  $\sim 50$  kpc of all four dark matter haloes from the Aquarius simulations are prolate with axial ratios of  $c \sim b \sim 0.7a$ . The ratios stay quite constant between  $z = 1.3$  and 1.0.

When a rigid disk is introduced, all three axes of the halo shorten in response to the added mass. This contraction is illustrated by the more closely spaced equidensity contours in the right column of Fig. 1, and by the shrinking length of the initial major axis in the right column of Fig. 2.

Despite the overall contraction of the inner halo in response to the disk, how the axial ratio of the halo is modified

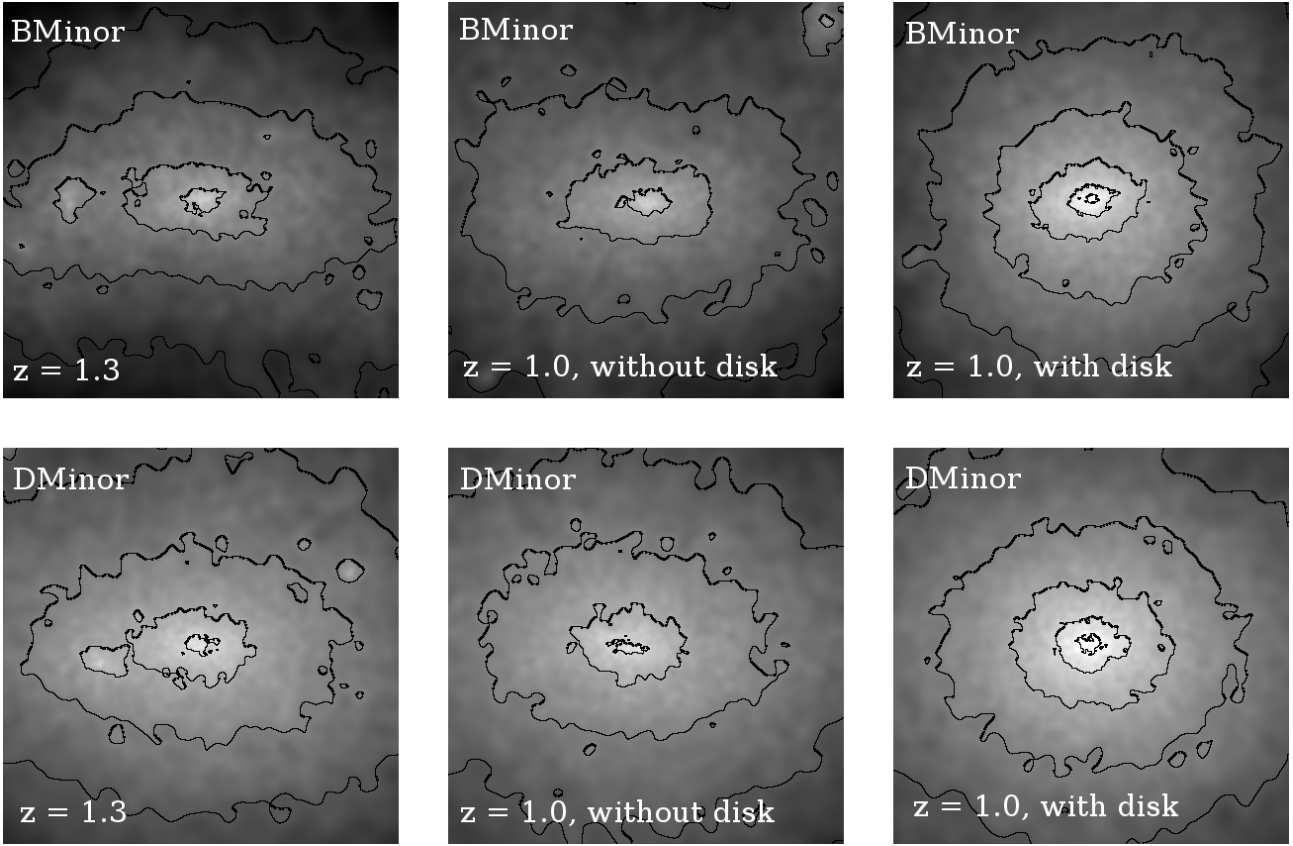


**Figure 1.** Surface density of the dark matter particles in halo B (top) and halo D (bottom), projected along their minor axes. The images are 40 kpc across. In the pure dark matter run without a disk (left and middle columns), the haloes are prolate (in the inner 40 kpc) and the shapes evolve little from  $z = 1.3$  to 1.0. However, when a rigid disk is introduced (with disk normal aligned with the minor axis) adiabatically between  $z = 1.3$  and 1.0 (right column), the dark matter haloes are symmetrized in the disk plane and become oblate by  $z = 1.0$ . The inner haloes also become denser as illustrated by the more closely spaced constant-density surfaces in the right column.

depends on the orientation of the disk. When the disk normal is initially aligned with the minor axis of the halo, we find the presence of the disk to nearly symmetrize the axial ratio of the dark matter halo in the disk plane, as shown by the rounder contours in the right column of Fig. 1. The solid curves in the upper panels of Fig. 2 show the corresponding evolution in the axial ratios:  $b/a$  evolves from  $\sim 0.7$  towards 0.9, while  $c/a$  remains relatively constant at  $\sim 0.6$  to 0.7 between  $z = 1.3$  and 1.0. The inner  $\sim 50$  kpc of the haloes therefore changes from being prolate to nearly oblate in the presence of a disk in the minor orientation.

When the disk normal is initially aligned with the major axis of the halo, the halo in the disk plane starts out quite symmetric since  $b \sim c$  at  $z = 1.3$ . As the solid curves in Fig. 2 show, the initial major axis  $a$  contracts much more in this orientation than in the minor orientation (right column) in the presence of the disk, increasing the axial ratios  $b/a$  and  $c/a$  but keeping the ratio of  $b/c$  relatively constant (left two columns). The haloes become nearly spherical at  $z \sim 1.2$ , after which the initial major axis becomes the minor axis as  $b/a$  and  $c/a$  both exceed unity. Note that for ease of comparison, we name the principal axes  $a, b, c$  (with  $a \geq b \geq c$ ) at  $z = 1.3$  and plot the subsequent evolution of the *same* axes. The haloes therefore evolve from being prolate to oblate in the presence of a disk in the major orientation. The difference here is the disk normal that was initially aligned

with the halo’s major axis at  $z = 1.3$  ends up being aligned with the halo’s minor axis at  $z = 1$ , and this occurs because of changes in the axial lengths of the halo rather than re-orientation of the disk.

Our results for the shapes of haloes without and with a stellar disk are in broad agreement with previous work. Dark matter haloes in  $N$ -body simulations generally have a range of shapes with a preference for prolateness over oblateness; the shapes can also depend on the radius, varying from prolate in the inner regions to triaxial or oblate in the outer parts (e.g., Frenk et al. 1988; Dubinski & Carlberg 1991; Warren et al. 1992; Cole & Lacey 1996; Jing & Suto 2002; Bailin & Steinmetz 2005; Allgood et al. 2006; Hayashi et al. 2007; Bett et al. 2007; Vera-Ciro et al. 2011). The presence of a disk in simulations has been shown to wash out the prolateness of the halo and make the inner haloes either more spherical or oblate (e.g., Dubinski 1994; Berentzen & Shlosman 2006; Debattista et al. 2008; Kazantzidis et al. 2010; Tissera et al. 2010; Abadi et al. 2010). An analysis of the characteristic frequencies of orbits in dark matter haloes Valluri et al. 2010 suggests that the change in halo triaxiality is due primarily to changes in the shapes of individual orbits of collisionless particles in response to a central baryonic component.

In addition to changes in the axial ratios, adding a stellar disk can also reorient the halo’s equipotential surfaces

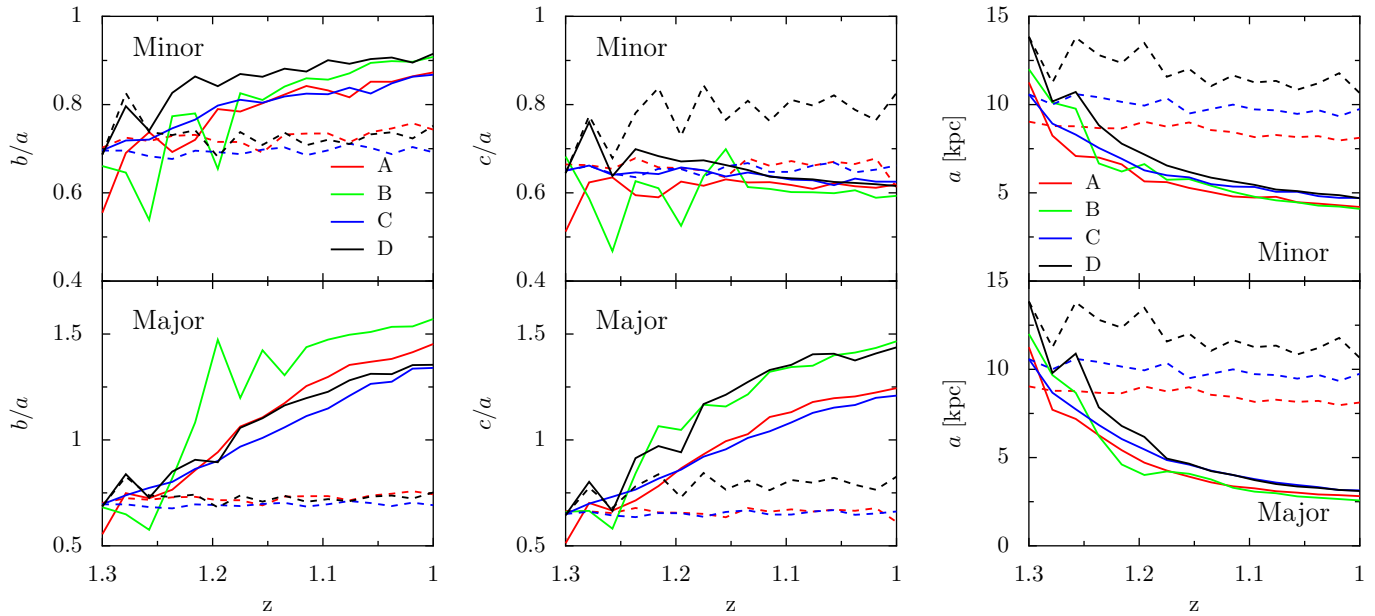


**Figure 2.** Effects of the growing rigid disks on the shapes of dark matter haloes between  $z = 1.3$  and  $1.0$ . The left and middle columns show the time evolution of the axial ratios  $b/a$  and  $c/a$ , respectively; the right column shows the effect of the disks on the initial major axis  $a$  (for a given equipotential surface) of the haloes. Within each panel, the dashed curves show the axes for the original Aquarius haloes A (red), B (green), C (blue), and D (black) between  $z = 1.3$  and  $1.0$ . The ratios stay nearly constant with  $c \sim b \sim 0.7a$ . The solid curves show how the insertion of a growing rigid disk between  $z = 1.3$  and  $1.0$  shrinks all three axes of the dark matter haloes and modifies the axial ratios. The modifications depend on whether the disk normal is initially aligned with the minor (top panels) or with the major (bottom panels) axis of the halo at  $z = 1.3$ . Since the axial lengths of the haloes change with time, the initial major and minor axes may not stay as the major and minor axes at all times. For ease of comparison, we name the principal axes  $a, b, c$  (with  $a \geq b \geq c$ ) at  $z = 1.3$  and plot the subsequent evolution of the *same* axes. The ratios  $b/a$  and  $c/a$  can therefore become greater than 1 at later times. The axial ratios for the original halo B are very noisy and are not plotted because a nearby subhalo twists its major axis as it falls into the halo.

between  $z = 1.3$  and  $1.0$ . Comparing the haloes in our simulations with disks and those in the original Aquarius simulations, we find that with the exception of halo B, the major axis of the halo does not experience significant reorientation in the presence of a growing disk. In halo B, a subhalo is visible at  $\sim 15$  kpc from the disk center at  $z = 1.3$  in Fig. 1. In the original Aquarius halo, this subhalo twists the major axis of halo B as it falls into the halo. The axial length for halo B is therefore quite noisy and is not plotted in Fig. 2. When a stellar disk is added, we find the major axis to be more stable due to the influence of the rigid disk.

#### 4 LIVE STELLAR DISKS, BARS, AND WARPS

In this section we present the results for the evolution of the live stellar disks in the Aquarius dark matter haloes from  $z = 1.0$  to  $0.0$ .

To determine the disk plane at each output, we bin the disk particles in radius, and draw an imaginary plane through the center of mass of the entire disk. The sum of the squared distances of each particle in the given bin to the plane is computed, and the normal to the plane is varied to minimize this sum. In this way, we find a disk normal for each radial bin of the disk. This process is performed for each output and a history of the disk’s orientation is constructed. As reported below, we find this procedure to produce disk normals that are nearly identical in the central region of the disk, but the outskirts can be warped and have a very

different orientation. We have also computed the angular momentum vector for each disk using all the disk particles. This vector is aligned to within 2 degrees with the normal of the inner disk.

#### 4.1 Structural Properties of Live Disks

Images of the final ( $z = 0$ ) surface densities of the live disks are plotted in Fig. 3. For completeness, we show both the face-on and edge-on views of each disk in the four haloes. The left two columns show the disks that are initially aligned with the minor axis of the halo; the right two columns show the major axis runs. The images (43 kpc on a side) clearly show that a bar extending to at least  $2R_d$  has formed in each disk, with the C disks containing the weakest bars, and the minor disks containing slightly longer bars than the major disks. We will further quantify the bar strength and evolution in § 4.2.

In addition to the bars, many edge-on disk galaxies in the local universe exhibit X-shaped structures or peanut-shaped bulges (e.g., Whitmore & Bell 1988; Kuijken & Merrifield 1995; Bureau & Freeman 1999; Bureau et al. 2006). These features are also seen in Fig. 3. Their existence may be related to the buckling of the bar that heats and ejects disk material (Combes & Sanders 1981; Raha et al. 1991; Mihos et al. 1995).

The edge-on images of the disks in Fig. 3 reveal a large variation in the amount of material out of the plane of the

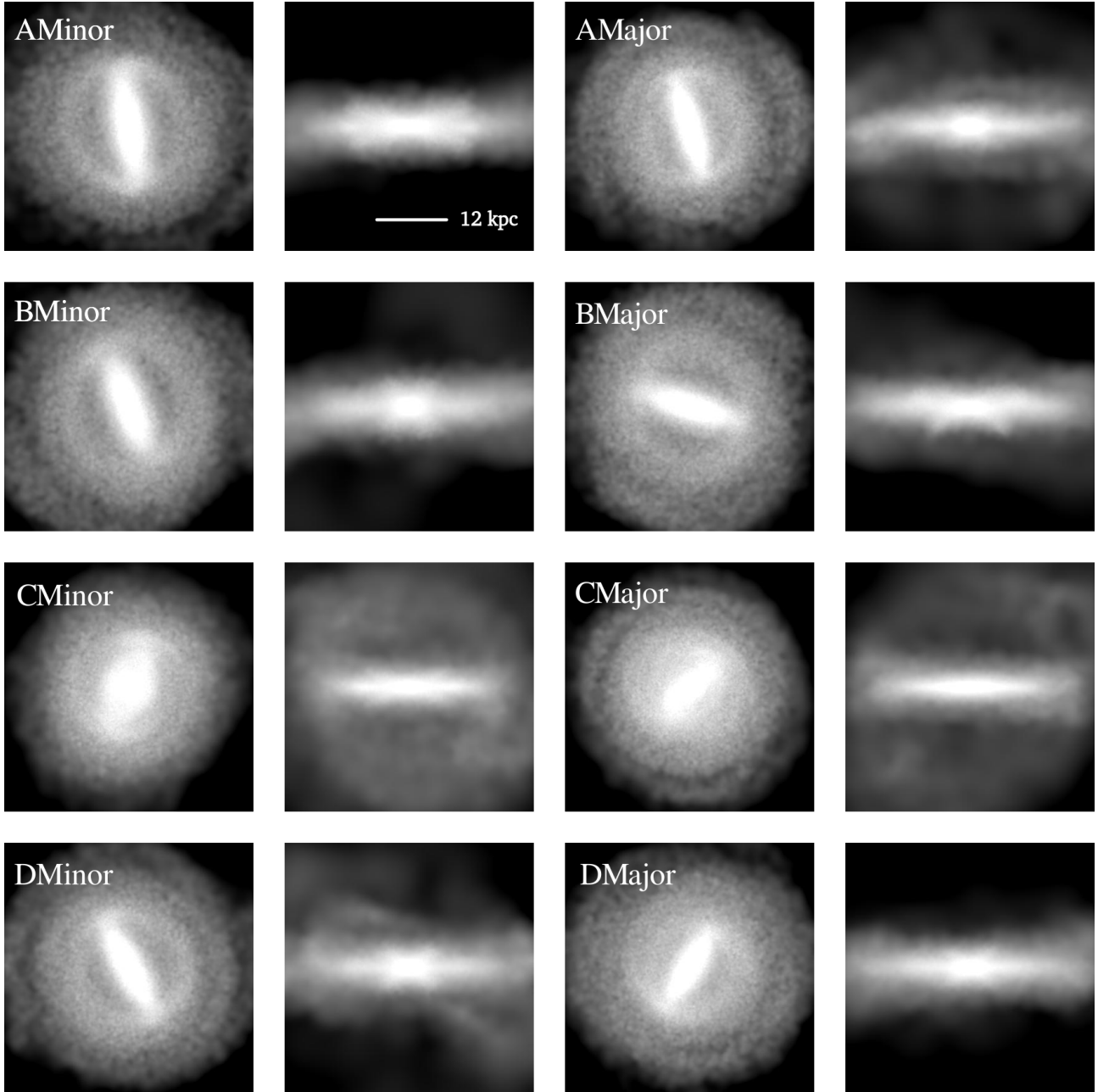


**Figure 3.** Surface density of the  $z = 0$  stellar disk, viewed faced-on (columns 1 and 3) and edge-on (columns 2 and 4), for haloes A, B, C and D (from top down). Each image is 43 kpc on a side. “Minor” and “Major” indicate whether the disk normal is initially aligned with the minor or major axis of the dark matter halo at  $z = 1.3$ .

disk. The CMinor, DMinor, AMajor, and CMajor haloes contain a prominent diffuse component of stars extending to tens of kpc outside the disk plane, whereas this component is nearly absent in the other four haloes. We will examine the kinematic properties of these stars in § 4.3 and the connection to the outer warps of the disk plane in § 4.4.

Fig. 4 shows snapshots of the disk surface density (left) and mean vertical height (middle) between  $z = 1$  and 0, and the  $z = 0$  vertical profile (right) for the four “Minor” disks (from top down). Fig. 5 shows the same quantities for the four “Major” disks. The central surface density of the disk in the left column is seen to increase with time when a

stellar bar forms. In addition, there is a slight enhancement at large radii in each case. This effect is most pronounced in the B disks and least pronounced in the C disks. The increase of material at large radii tends to increase the best fit scale length  $R_d$  of the disk, but we find the effect to be at most at the  $\sim 20\%$  level:  $R_d$  increases from the initial value of 3 kpc at  $z = 1$  to 3.4, 3.7, and 3.3 kpc at  $z = 0$  for haloes A, B, and D, respectively. The scale length for halo C, by contrast, stays remarkably constant. We note, however, that the surface density profiles of the B and D disks in Figs. 4 and 5 at the end of the simulations deviate significantly from the initial single exponential form.

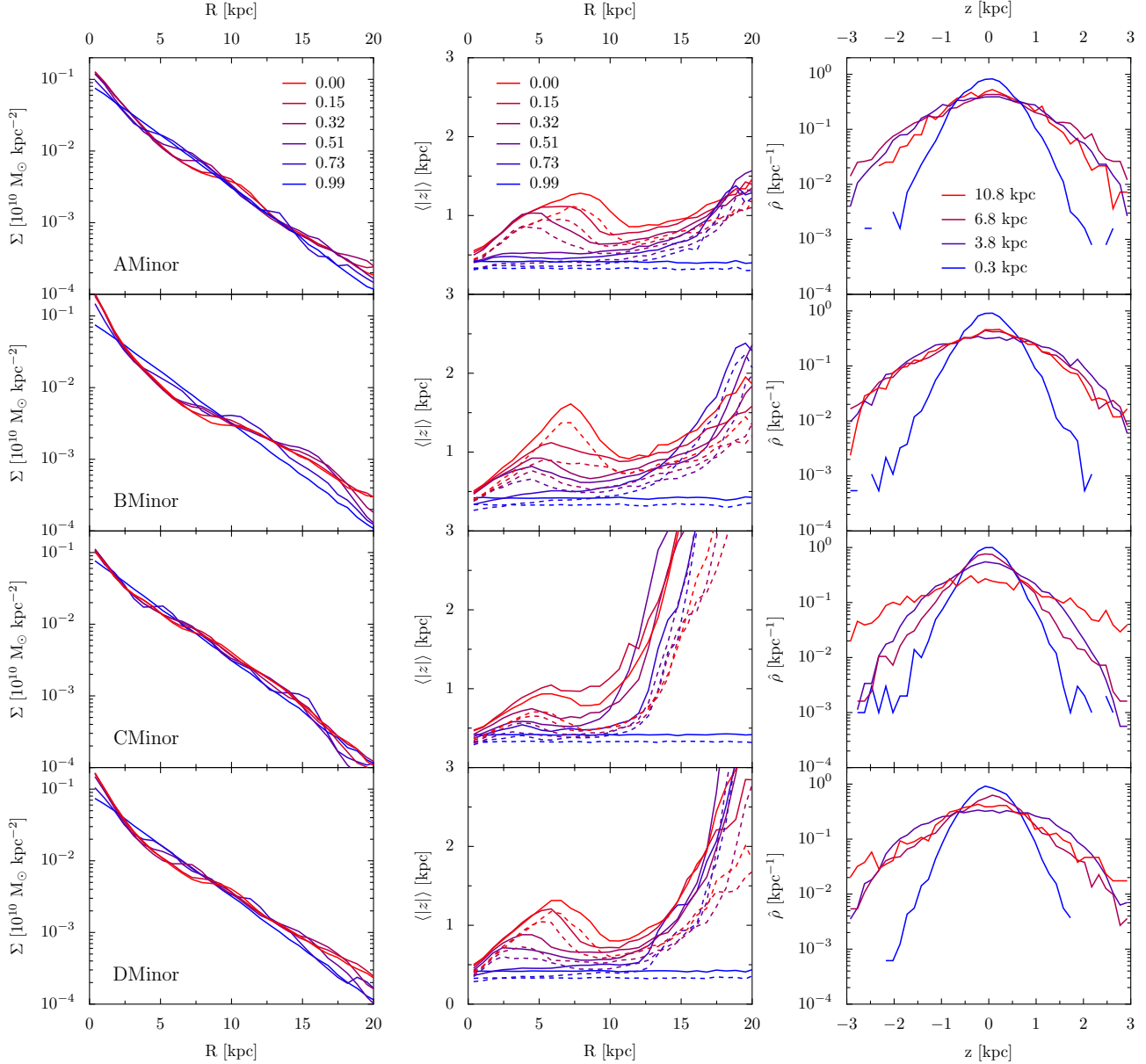


**Figure 4.** Structural properties of the disks in the minor orientation for haloes A, B, C, and D (top down). The projected surface density of the disk as a function of radius (left column) is quite stable between  $z = 0.99$  (blue) and  $0.0$  (red), with a steepening in the inner few kpc due to the stellar bars. The middle column shows two measures of the height of the disk, the mean (solid) and median (dashed) distance of the disk particles from the disk plane, as a function of radius for six redshifts during the simulations. The vertical profiles of the disk at  $z = 0$  (right column) become broader with increasing radii.

The middle and right columns of Figs. 4 and 5 show the vertical structures of the disks. The radial profile of the mean and median vertical height  $|z|$  is flat at the first two snapshots ( $z = 0.99$  and  $0.73$ ) for all eight disks, A, B, D as a bar forms. The outer profile of  $|z|$  at  $R \gtrsim 10$  kpc also varies greatly from disk to disk. A dramatic rise in  $|z|$  is seen in the outer parts of CMinor, DMinor and CMajor, and to a lesser extent, AMajor. This rise correlates directly with the amount of material out of the disk plane in Fig. 3. Throughout the simulation, the disk plane changes orientation. While most of this reorientation is a coherent tumbling motion of the disk, some of the outermost material

gets ‘left behind,’ creating streams that are on a different plane than the bulk of the disk mass. More discussion will be presented in § 4.4.

The CMajor disk is remarkable in that among the eight disks, it experiences the least amount of vertical thickening and heating in the inner 10 kpc but contains the largest amount of material out of the disk plane at large radii. These results strongly suggest that the features at the centers of these disks and the outer material are formed from separate mechanisms. We present evidence below that the thickening at the center of the disk is due to a large bar that develops, whereas the material out of the plane is due to disk warping



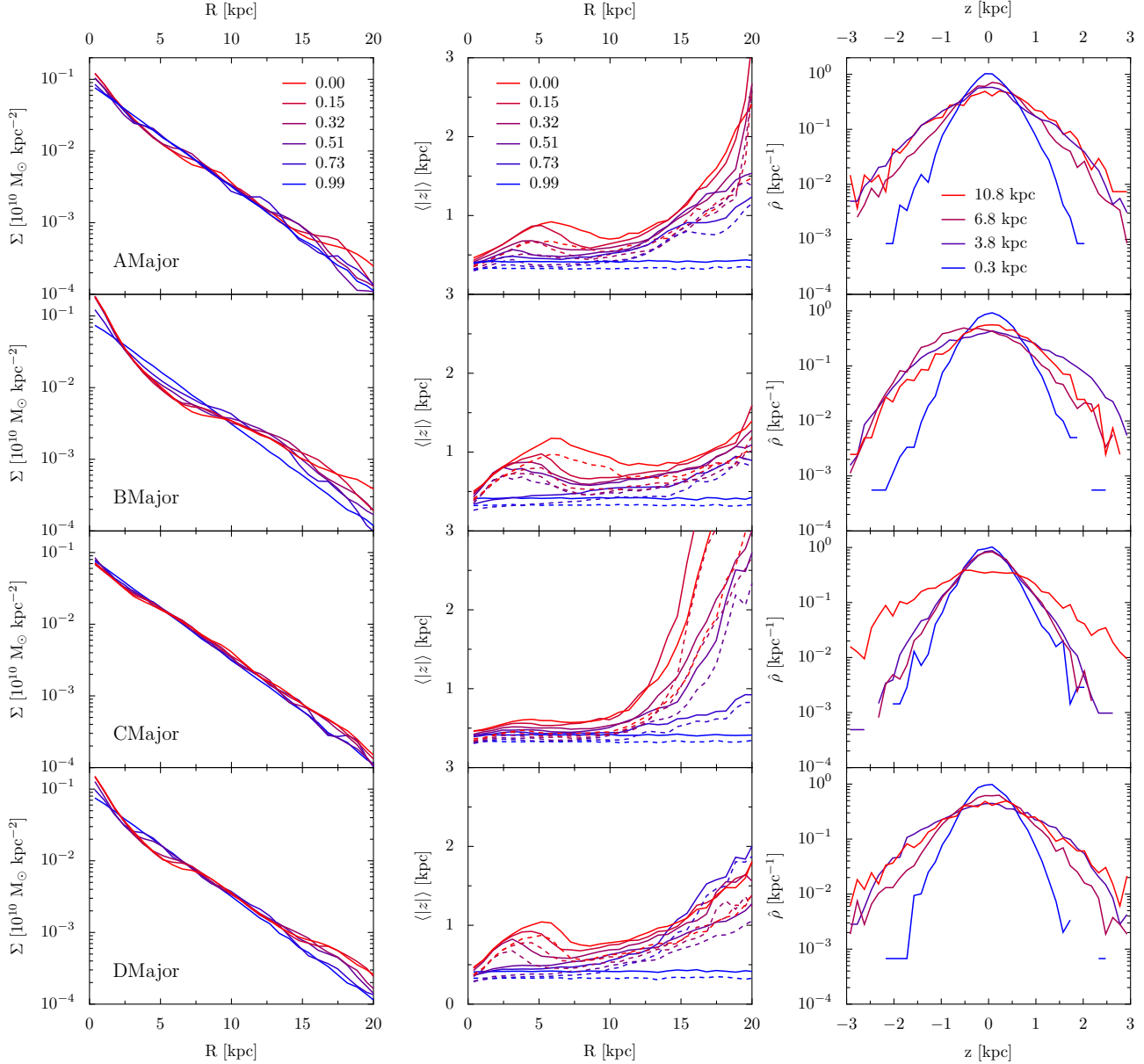


**Figure 5.** Same as Fig. 4 but for the disks whose normal is initially aligned with the major axis of the halo at  $z = 1.3$ .

that results from misalignment in the inner and outer parts of the halo.

## 4.2 Stellar Bars

To quantify the bars that formed in the central regions of the disks, we compute the strength of the  $m = 2$  Fourier amplitude of the surface density of each disk. The particles in the disk are binned radially in the disk plane, and the following coefficients are computed for each bin:

$$\begin{aligned} a_m &= \sum_i \cos(m\theta_i) & m = 0, 1, \dots \\ b_m &= \sum_i \sin(m\theta_i) & m = 1, 2, \dots \end{aligned} \quad (3)$$

where the sum is carried out over all the disk particles (labeled by  $i$  and assumed to have equal mass) in the radial bin, and  $\theta_i$  is the azimuthal position of that particle in the disk plane. The strength of a given mode is  $c_m = \sqrt{a_m^2 + b_m^2}$ . To quantify the strength of the  $m = 2$  mode for the whole disk, we compute the relative mode strength  $A_2$  by integrating  $c_2$  over the inner two scale radii:

$$A_2 = \frac{\int_0^{2R_d} c_2(R) R dR}{\int_0^{2R_d} c_0(R) R dR}. \quad (4)$$

Fig. 6 shows the evolution of  $A_2$  computed over the inner  $2R_d$  for disks in both the minor orientation (top) and the major orientation (bottom). The amplitude of  $A_2$  matches the expectation from examining the images in Fig. 3. In particular, the bar is weakest in the CMajor halo, with  $A_2 \lesssim 0.1$  for most of the simulation. The CMinor disk is also distinctly

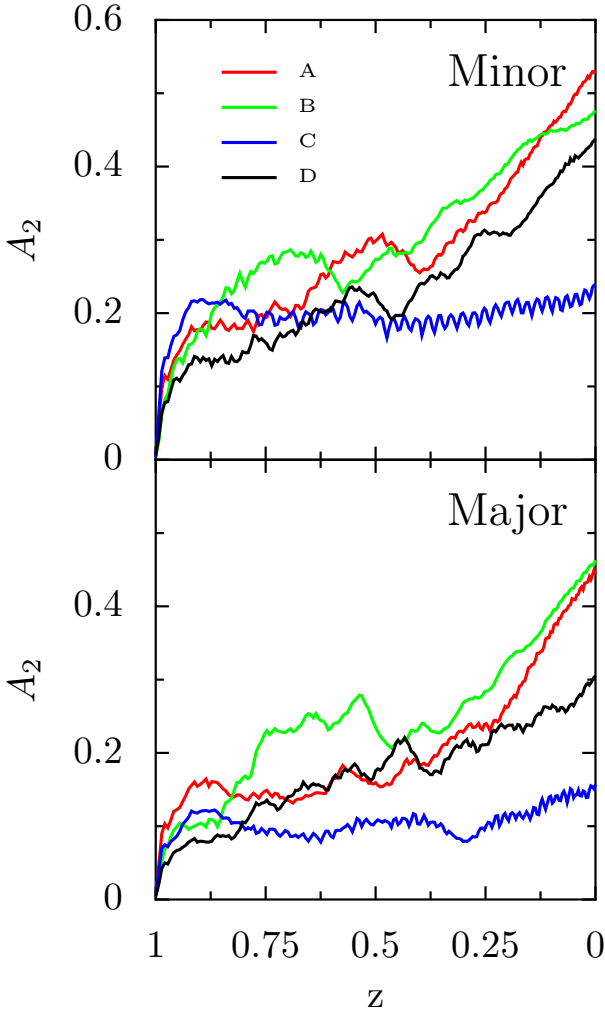


**Figure 6.** Strengths of stellar bars measured by the  $m = 2$  mode,  $A_2$ , in the inner  $2R_d$  for the disks in each halo for the minor (top) and major (bottom) orientations. Halo C (blue) develops the weakest bar, while the  $m = 2$  mode grows with time for haloes A (red), B (green), and D (black).

stable, in which  $A_2$  stays nearly a constant at  $\approx 0.2$  after a rapid initial rise from 0 to 0.2.

In contrast to halo C, the bar strengths  $A_2$  for haloes A, B, and D show a rapid initial rise from zero, followed by a  $\sim 20$  to 30% drop in amplitude at a redshift that differs from disk to disk, and then a late time growth leading to a final value as high as  $A_2 \sim 0.5$  at  $z = 0$ . The dips in  $A_2$  after initial bar formation have been attributed to bar buckling instability in earlier studies such as the idealized disk and halo systems of Dubinski et al. (2009) and the constrained cosmological run of Villa-Vargas et al. (2009). For our disks in the initial minor orientation (top panel in Fig. 6), BMinor shows the earliest dip at  $z \approx 0.65$ ; the dips in  $A_2$  for DMinor and AMinor start to occur at  $z \approx 0.5$ . For our disks in the initial major orientation, only BMajor and DMajor exhibit noticeable dips in  $A_2$  at  $z \approx 0.55$  and  $0.45$ .

To quantify the bar buckling instability further, we discuss in the next subsection and show in Fig. 7 the corresponding vertical heating measured by the relative disk velocity dispersion in the vertical direction in the inner  $2R_d$  of

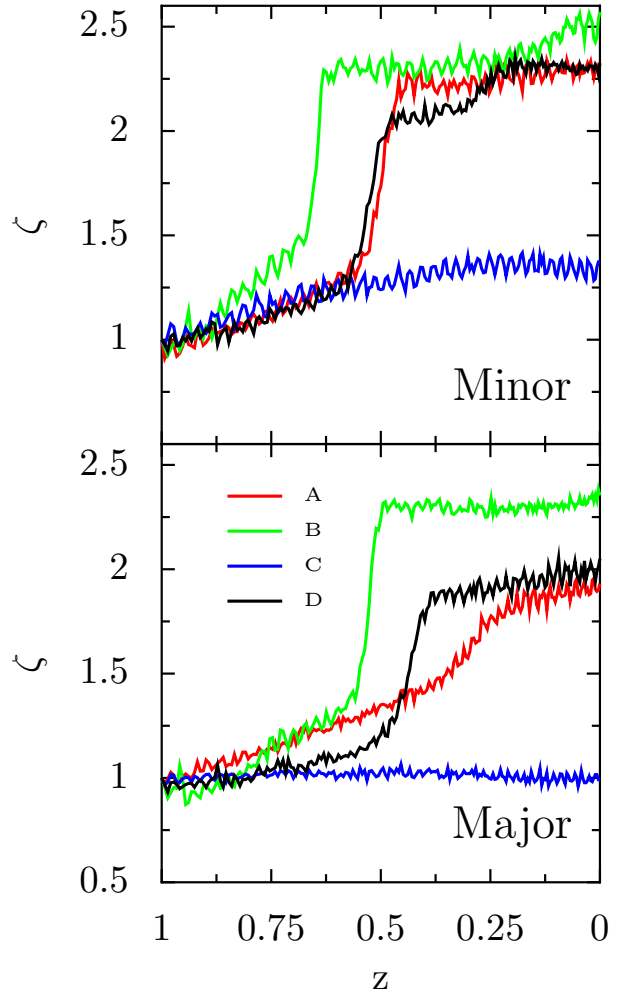


**Figure 7.** Evolution of the vertical heating parameter  $\zeta$  (defined in eq. (6)) for the disks in the minor (top) and major (bottom) orientations. The disks that form a strong bar, which eventually buckles, all show a large jump in  $\zeta$  during buckling. The two C disks have the weakest bars and show little heating.

the disk. For the five disks AMinor, BMinor, DMinor, BMajor, and DMajor, there is a clear sharp rise in disk heating at the redshift at which  $A_2$  dips in Fig. 6.

The formation of bars in these disks is not entirely unexpected based on the criterion of Efstathiou et al. (1982). According to this criterion, the disk will be stable against developing a bar if

$$Q_{bar} = \frac{v_M}{\sqrt{M_d G/R_d}} > 1.1, \quad (5)$$

where  $v_M$  is the maximum velocity of the rotation curve, and  $M_d$  and  $R_d$  are the disk mass and scale length, respectively. For the initial live disks in our simulations at  $z = 1.0$ , we find  $Q_{bar} = 0.98, 0.83, 1.03$ , and  $0.93$  for haloes A, B, C, and D, respectively, and the value of  $Q_{bar}$  is largely independent of the initial disk orientation (see Table 1 for the full list). Since the same disk is used for all four haloes, the values of  $Q_{bar}$  reflect the differences in  $v_M$ , which in turn depends on the masses of the haloes at  $z = 1.0$ :  $M_{vir} = 1.03 \times 10^{12}$ ,  $5.7 \times 10^{11}$ ,  $1.18 \times 10^{12}$ , and  $1.07 \times 10^{12} M_\odot$  for haloes A, B, C, and D, respectively. Since  $Q_{bar} < 1.1$ , these disks are expected

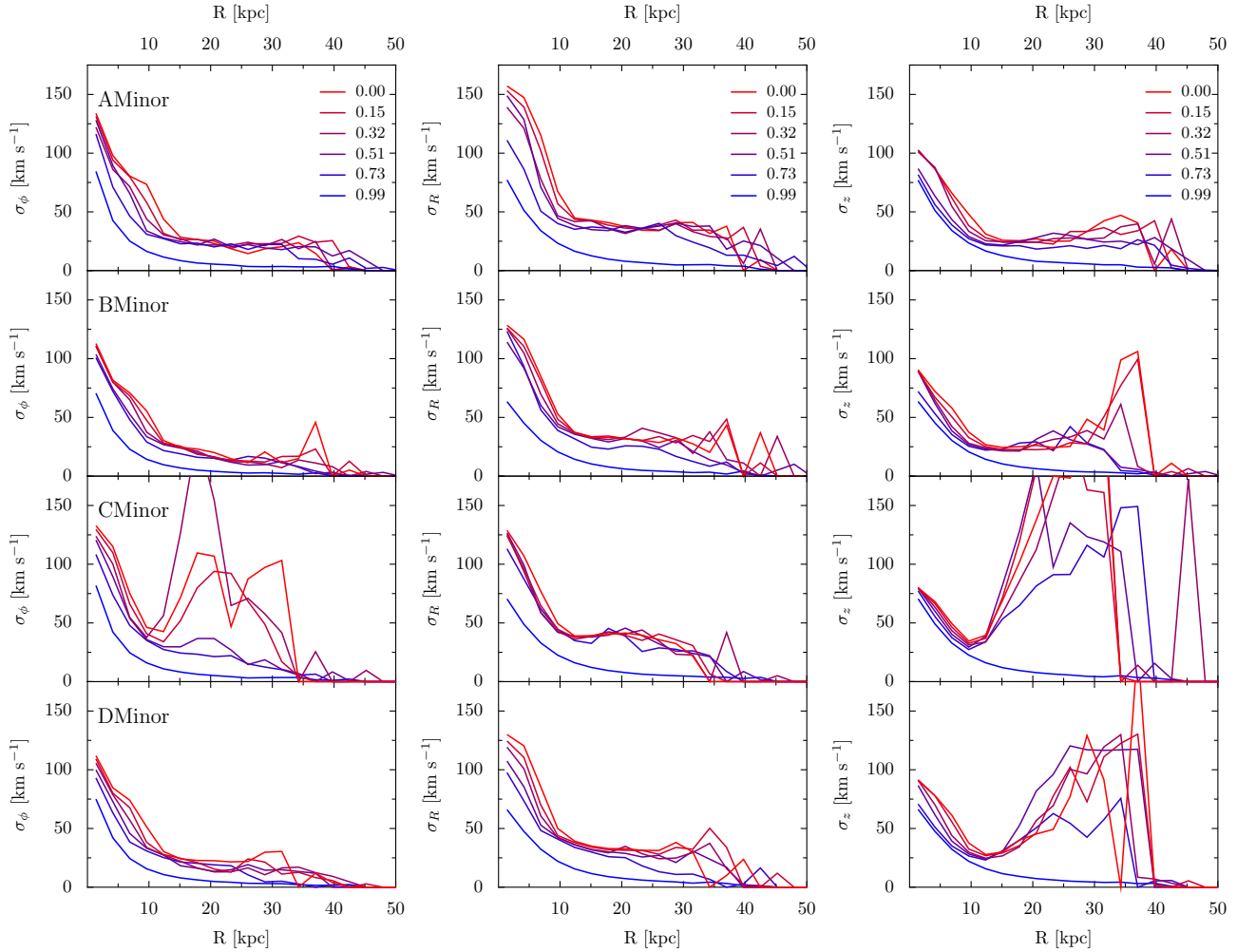


**Figure 8.** Velocity dispersion profiles of the minor disks in haloes A, B, C and D (from top to bottom). The three columns show the three velocity components defined by the disk: azimuthal (left), radial (middle), and vertical (right). In each panel, the different curves show six outputs ranging from  $z = 0.99$  (blue) to 0.0 (red).

to be unstable against a bar forming, which is indeed in qualitative agreement with Fig. 3. Halo C has the weakest bar since it is the most massive halo and its  $Q_{bar}$  value is closest to the threshold for stability.

In comparison, we find  $Q_{bar}$  to be greater than 1.1 in our simulations in which the disk masses are lowered by a factor of 2 and 3 (see Sec. 5 below); the corresponding  $Q_{bar}$  is 1.13 and 1.23 for halo A, and 1.15 and 1.26 for halo C, respectively. The increase in  $Q_{bar}$  for decreasing disk mass indicates stronger stability against bar formation in lower mass disks. These smaller disks indeed appear mostly free of bars, as shown below in Fig. 12. The  $m = 2$  coefficient is also small, with  $A_2 < 0.2$  (right panels of Fig. 13). Equation (5) is approximate since it treats only the self-gravity of the disk and does not consider the velocity dispersion (Athanasoula 2008). For the disks studied here, however, equation (5) appears to provide a reasonable approximation for bar stability.

Stellar bars have been reported to dissolve in live triaxial dark matter haloes (e.g., Berentzen et al. 2006). As the solid curves in Fig. 2 show, our haloes at the end of the disk growth phase at  $z = 1.0$  are all triaxial with fairly sim-

ilar axial ratios. For instance, the axial ratios of the AMajor and AMinor haloes at  $z = 1.0$  are 1.00:0.86:0.69 and 1.00:0.87:0.62, respectively, while the CMajor and CMinor haloes have 1.00:0.90:0.61 and 1.00:0.87:0.62, respectively. The A disks form bars that buckle and then continue to grow until  $z = 0$ , but the C disks never form appreciable bars and the  $A_2$  amplitude stays nearly constant and low. Therefore, halo triaxiality in our simulations appears to play a minor role in bar evolution in comparison to other factors such as the relative disk-to-halo mass.

### 4.3 Disk Heating and Velocity Profiles

In addition to the shape of the disk, the velocity structure of the disk evolves during the simulation. We define the following quantity to characterize the vertical heating of the disk. For a cumulative radial disk mass profile  $M(R)$  and a vertical velocity dispersion profile  $\sigma_z(R)$ , we use

$$\zeta = \frac{\int_0^{2R_d} \frac{dM}{dR} \sigma_z^2(R) dR}{\int_0^{2R_d} \frac{dM_0}{dR} \sigma_{z,0}^2(R) dR} \quad (6)$$

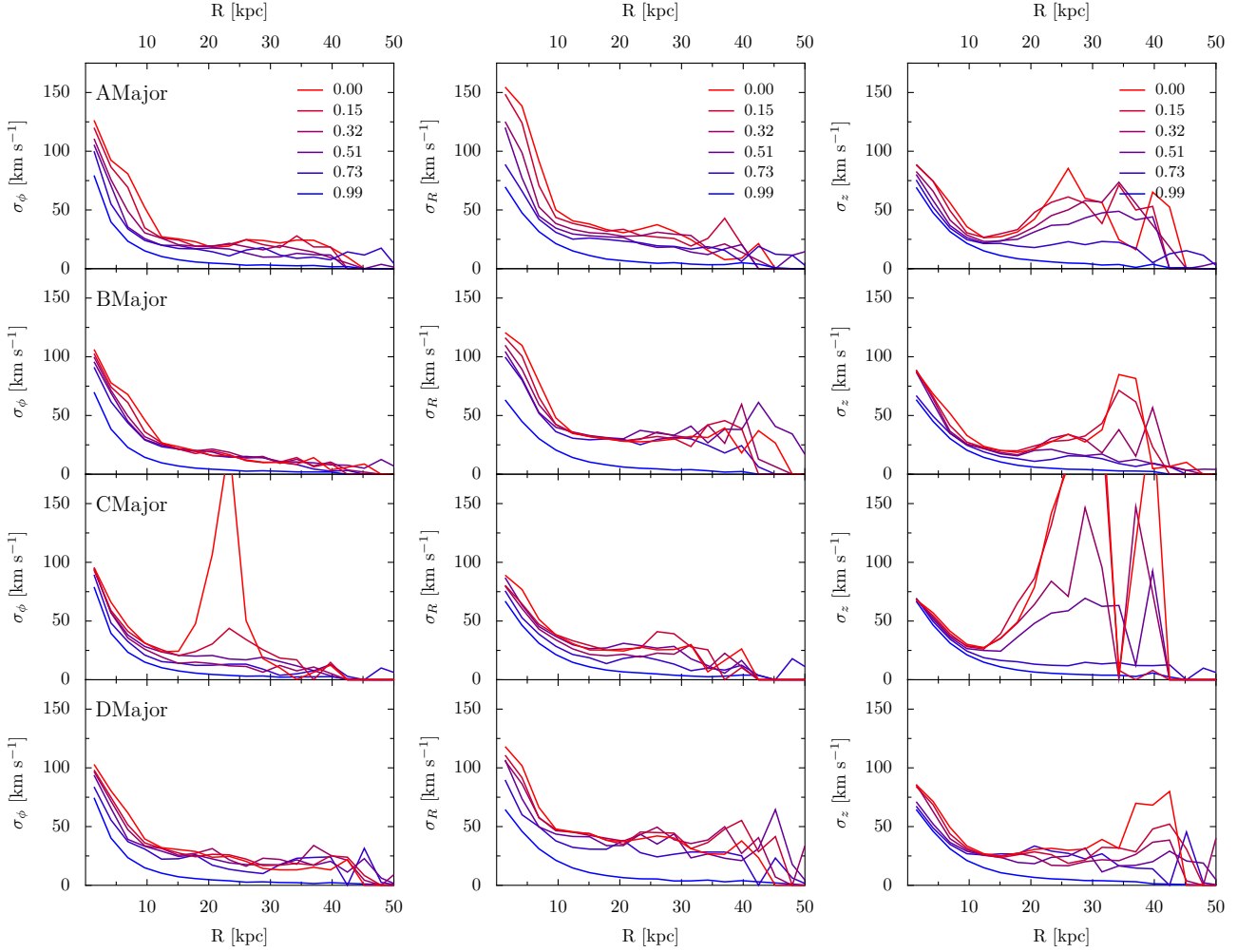


**Figure 9.** Same as Fig. 8 but for the four disks in the major orientation.

where subscript “0” in the denominator denotes that these quantities are evaluated for the initial redshift of the live phase ( $z = 1.0$ ). The limit of integration is set to twice the scale radius, as in the  $A_2$  definition above.

The evolution of  $\zeta$  with redshift is given in Fig. 7 for disks in the minor (top) and major (bottom) orientations. The halo-to-halo variation is striking. Once again, vertical heating is negligible in the CMajor disk, in which  $\zeta$  stays at unity throughout the simulation. The CMinor disk experiences a gradual increase of only  $\sim 30\%$  in  $\zeta$  between  $z = 1$  and 0. By contrast,  $\zeta$  jumps from 1 to 2–2.5 suddenly at  $z \sim 0.5$  to 0.7 for the disks in the other three haloes. This jump in  $\zeta$  is accompanied by a dip in the bar strength  $A_2$  at a similar redshift, as a result of bar buckling (see Fig. 6 and previous subsection).

The complete set of profiles of the stellar velocity dispersions in three directions about the disk plane is shown in Fig. 8 and 9 for the disks in the minor and major orientation, respectively. In each figure, the three columns show the azimuthal (left), radial (middle), and vertical (right) components of the stellar velocity dispersion. Within each panel, six snapshots between  $z = 1$  and 0 are plotted.

In the vertical direction in the inner  $R \sim 10$  kpc of the disk, jumps in  $\sigma_z$  are clearly seen between  $z \sim 0.7$  and 0.5

for the five disks AMinor, BMinor, DMinor, BMajor and DMajor, as was shown in Fig. 7. For the other three disks, AMajor’s  $\sigma_z$  at small  $R$  increases more gradually without a sudden jump, while  $\sigma_z$  stays nearly constant for CMajor and CMinor, which do not form a significant bar. This behavior is again consistent with Fig. 7.

In the vertical direction at radii beyond 10 kpc, some disks show a sharp increase in  $\sigma_z$  in Figs. 8 and 9. The rise is particularly prominent for the three disks CMinor, DMinor, and CMajor, in which  $\sigma_z$  reaches  $\gtrsim 150$  km/s at  $R \sim 20$  to 40 kpc. The edge-on images in Fig. 3 indeed show that these three disks contain an extended diffuse component of stars outside the disk plane, spreading to tens of kpc. This component gives rise to the sharp increase in the mean vertical height in the three objects in Figs. 4 and 5. The AMajor disk also exhibits a similar behavior to a lesser extent. The AMinor disk, by contrast, stays thin and cold in the outer part despite the strong bar formed in the inner region.

In the radial and azimuthal directions, Figs. 8 and 9 show two phases of heating. Between the first two snapshots at  $z = 0.99$  (blue curves) and 0.73 (light purple curves), which precedes any bar formation,  $\sigma_R$  and  $\sigma_\phi$  in the inner 10 kpc increase for all eight disks, with a larger jump for the disks in the minor orientation. In comparison, there is almost

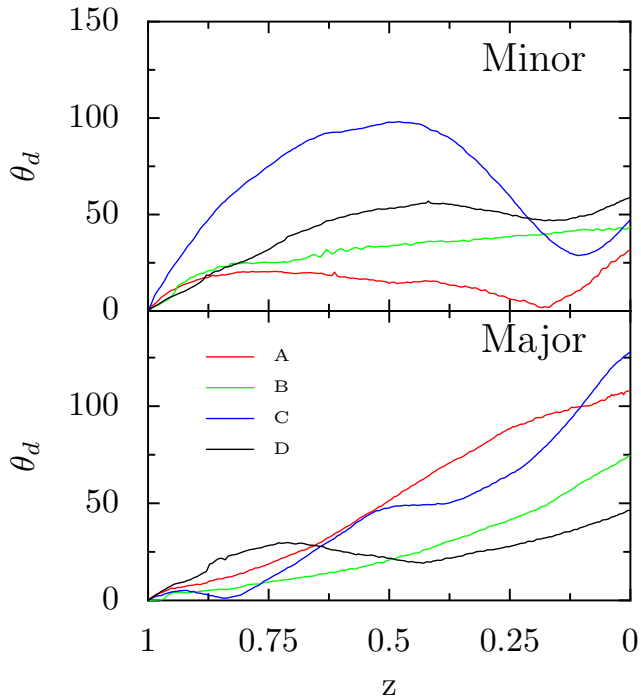


**Figure 10.** Angle (in degrees),  $\theta_d$ , between the disk normal (for the inner 5 kpc) at a given redshift and the disk normal at  $z = 1.0$  for haloes A (red), B (green), C (blue), and D (black). The disk normal is initially aligned with the minor (top) or major (bottom) axis of each halo at  $z = 1.3$ . The disks experience drastically different amounts of tumbling between  $z = 1.0$  and  $0$ : the two C disks and AMajor disk rotate by more than 100 degrees, whereas the normal of the AMinor disk stays within  $\sim 20$  degrees throughout the simulation.

no vertical heating as evidenced by the nearly identical  $\sigma_z$  at these snapshots. Similar trends are reported in an idealized model for the halo and disk of M31, in which the changes in  $\sigma_R$  and  $\sigma_\phi$  are attributed to transient spiral features present early in the simulations (Gauthier et al. 2006).

A second phase of heating in the radial and azimuthal directions can be seen in a subset of disks in the inner  $\sim 10$  kpc in the  $z < 0.73$  snapshots of Figs. 8 and 9. It is tempting to attribute this phase of heating to bar activities, e.g.,  $\sigma_R$  and  $\sigma_\phi$  are nearly unchanged between  $z = 0.73$  and  $0.0$  for CMinor and CMajor that have very weak bars, whereas they increase by up to 50% for AMinor and AMajor that have strong bars. Fig. 6 of Gauthier et al. (2006) illustrates similar heating and explains it by the stellar bars that have formed in their runs with dark matter subhalos. We note, however, that the BMinor disk (and BMajor to a lesser extent) contains a strong bar, but its  $\sigma_R$  and  $\sigma_\phi$  stay nearly constant after  $z = 0.73$ .

#### 4.4 Disk Reorientation and Warps

Once the stellar disk goes live at  $z = 1.0$  in our simulations, the orientation of the disk is free to change. The outer parts of the disks ( $R \gtrsim 10$  kpc) can experience significant warps compared with the inner parts, so we examine the two regions separately here.

For the central region, we plot in Fig. 10 the angle,  $\theta_d$ ,

between the disk normal computed from stars within 5 kpc at a given redshift and the initial disk normal at  $z = 1.0$ . The results do not depend sensitively on the choice of 5 kpc and are nearly identical when stars out to  $\sim 10$  kpc are included. The CMinor, CMajor, and AMajor disks are seen to experience the largest amounts of re-orientation by  $z = 0$ , but  $\theta_d$  evolves differently for each case. The CMinor disk normal starts to tilt away from its initial direction at  $z = 1$  immediately, reaching a separation of  $\sim 100$  degrees at  $z \sim 0.5$ . The CMajor disk orientation, on the other hand, stays quite constant until  $z \sim 0.7$ , after which  $\theta_d$  grows steadily and reaches  $\sim 125$  degrees at  $z = 0$ . AMajor resembles CMajor with  $\theta_d$  reaching  $\sim 110$  degrees at  $z = 0$ .

In comparison, the central regions of the AMinor and DMajor disks experience the least amounts of re-orientation. The disk normal for each case stays within  $\sim 20$  degrees throughout most of the simulation, and rises only slightly to  $\sim 30$  and  $45$  degrees, respectively, at  $z \sim 0$ .

We have also computed the relative orientation between each disk normal shown above and its halo at a given time. The principal axes of a halo are determined by binning the halo particles in gravitational potential and fitting ellipsoids to equipotential surfaces. This procedure is repeated at each bin in potential, which corresponds roughly to a given radius. In nearly all cases, the halo axes show very little twist over the inner 50 kpc, and the disk orientation (within 5 kpc) is very well aligned with one of the halo’s principal axes. Thus, when a disk re-orient in Fig. 10, it is doing so with the inner halo. Bailin & Steinmetz (2005) and Bailin et al. (2005) have reported similar internal alignment in haloes’ axes in N-body simulations and close alignments between disks and the inner haloes in hydrodynamical simulations.

Visual inspection of the stars at large radii suggests that the material is largely in the form of rings of material concentric with the disk rather than in a random diffuse form. These ring-like structures are, however, warped and offset from the inner disk. To quantify the relative orientation of the inner and outer parts of each disk, we plot in Fig. 11 the warp angle,  $\theta_{warp}(R)$ , which is defined to be the angle between the disk normal for the central radial bin and the normal for the bin at radius  $R$ . For each disk, this angle measured at three redshifts,  $z = 1, 0.5$ , and  $0.0$ , is shown. Initially ( $z = 1.0$ ; dotted lines), the disk is completely coherent by construction and  $\theta_{warp} = 0$  at all radii. As the disk evolves to  $z = 0.5$  (dashed) and  $z = 0.0$  (solid), a subset of the disks is significantly beyond 10 kpc.

The trends in Fig. 11 are closely correlated with those in Fig. 10: disks (and their haloes) such as CMinor, CMajor, and AMajor that have tumbled significantly between  $z = 1$  and  $0$  develop large outer warps by  $z = 0$ , whereas the disks with nearly constant normals such as AMinor and DMajor stay coplanar with  $\theta_{warp}(R) \lesssim 20$  degrees out to  $R = 30$  kpc. The time of the tumbling and warping is also correlated. For instance, the disk that starts to tumble earliest, CMinor, shows significant warping at the  $z = 0.5$  snapshot already, whereas  $\theta_{warp}$  for the CMajor disk is less than 20 degrees at  $z = 0.5$  but rises to  $\sim 70$  degrees at  $z = 0$ .

The behavior above also matches the expectation from Figs. 3, 4 and 5: the larger the value of  $\theta_{warp}$ , the more material appears out of the plane of the disk, and the larger the increase in the disk height at large radii.

While the inner parts of the halo and disk are well

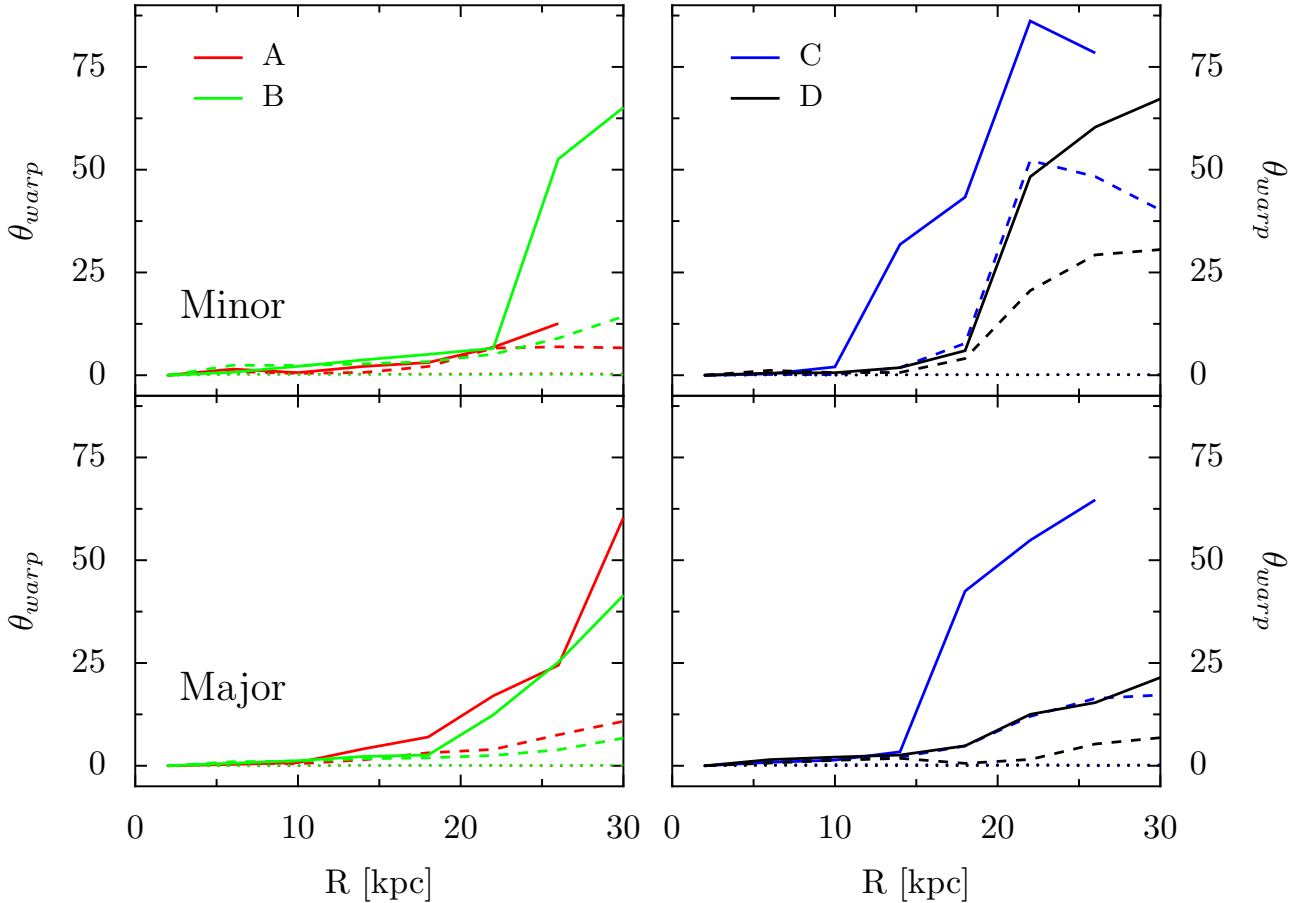


**Figure 11.** Warp angle for the Minor (top row) and Major (bottom row) disks as a function of radius at three different times:  $z = 1.0$  (dotted),  $0.5$  (dashed), and  $0.0$  (solid). The disk is flat at  $z = 1.0$  by construction so  $\theta_{warp} = 0$  at all radii. The BMinor, CMinor, DMinor, and CMajor disks show outer warps with  $\theta_{warp} > 60$  degrees at  $z = 0$ , whereas the AMinor and DMajor disks stay quite coplanar out to  $\sim 30$  kpc.

aligned, the outer region of the halo can be misaligned with the inner region (Bailin et al. 2005). As the halo tumbles slowly over the course of the simulation, any such misalignment can generate tidal fields that torque the disk and cause the more fragile outer parts of the disk to warp (Debattista & Sellwood 1999; Dubinski & Chakrabarty 2009). We have compared the directions of the major and minor axes of each halo in the inner 50 kpc versus between 50 kpc and 100 kpc at various redshifts. We find the axes to be well aligned without much twisting, similar to the results reported in Vera-Ciro et al. (2011). The warps in our simulated disks therefore appear to be more correlated with the overall tumbling of the disk-halo system in the cosmological simulation. Other mechanisms have been shown to induce disturbances in the outer disk. Perturbations from infalling satellites or cold gas, for instance, can be sources of warping torques (e.g., Ostriker & Binney 1989; Quinn et al. 1993; Debattista & Sellwood 1999; Jiang & Binney 1999; Weinberg & Blitz 2006; Chakrabarti & Blitz 2009; Roškar et al. 2010). The satellites generate additional tidal fields and also bring in angular momentum that can alter the alignment of the disk and halo. The infalling cold gas can be strongly torqued by the hot gas halo. These mechanisms may act in concert on the outskirts of disks.

## 5 ALTERNATE DISK MODELS

To quantify the dependence of the disk structures on the assumed disk mass, we have performed additional simulations for halos A and C, in which the disk mass is reduced from the fiducial value of  $5 \times 10^{10} M_{\odot}$  by a factor of 2 and 3. The scale radius of the disk is reduced according to the observed scaling relation  $R_d \propto M_d^{1/3}$  (Shen et al. 2003). These runs are labeled “Half” and “Third” in Table 1. The change of disk mass required the disk growing phase between  $z = 1.3$  and  $1.0$  to be redone for each case since the dark matter haloes would be responding to the potential of a smaller and less massive disk.

We have also performed test runs with haloes A and C in which the disk is assumed to have an initial gas fraction of  $f_g = 0.4$ . These runs are labeled AMinorGas and CMinorGas. The total baryonic mass is the same as in the fiducial run, i.e.  $5 \times 10^{10} M_{\odot}$ ; the disk mass in stars is therefore reduced to  $3 \times 10^{10} M_{\odot}$ . The gas has the same radial profile as the stellar particles, but is set up to be in vertical hydrostatic equilibrium. For simplicity it does not form stars or cool. We include this component to test if a gas component helps stabilize the stars in a disk. A more realistic simulation will turn most of the gas at  $z = 1$  into stars by  $z = 0$ ,

thereby bracketing our results for the AMinorGas run and the fiducial run AMinor.

We find large reductions in the bar strengths as the disk mass is lowered. Fig. 12 shows the  $z = 0$  face-on surface density of the inner 21 kpc by 21 kpc region of four different disks for halo A. The right column of Fig. 13 shows the time evolution of the amplitude  $A_2$  of the  $m = 2$  mode that characterizes the bar strength for haloes A and C (see Sec 4.2). These figures show a clear decrease in bar strengths as the disk mass is reduced. Halo AMinor with the fiducial mass disk has a growing  $m = 2$  mode throughout the simulation, while the other three smaller disks all have  $A_2 < 0.2$ . The less massive disks in the C haloes also have smaller values of  $A_2$ , but the overall decrease is smaller as the CMinor disk shows at most a weak bar to begin with. As discussed in Sec 4.2, the approximate bar instability criterion given by equation (5) requires  $Q_{bar} < 1.1$  for bar formation. The value of  $Q_{bar}$  for each disk at  $z = 1.0$  is listed in Table 1. The disks with the fiducial mass of  $5 \times 10^{10} M_\odot$  satisfy this condition and indeed develop bars by  $z = 0$  (see Fig. 3). In comparison, the disks with reduced masses all have  $Q_{bar} > 1.1$  and  $A_2 < 0.2$  and show no strong bars.

The middle column of Fig. 13 shows the mean vertical distance of the stellar particles from the disk plane as a function of radius for these same simulations at  $z = 0$ . Both the height and radius are scaled to the initial disk size to aid in the comparison among disks with different masses. In the inner part of the disk, the bumps in  $|z|$  at two to three scale radii due to the bars in the fiducial disks are absent in the lower mass disks, consistent with the lack of bars in the latter. In the outer part of disk, the less massive disks are more easily brought out of the disk plane, leading to streamers that are originally closer to the center of the disk.

In contrast to the strong dependence of bar strengths on disk mass, we find the less massive disks to have similar effects as the fiducial disk on the dark matter halo between  $z = 1.3$  and 1.0 as the rigid disk is introduced. The left column of Fig. 13 shows that the axial ratio  $b/a$  for both haloes A and C is driven towards unity, while  $c/a$  is largely preserved as the rigid disk is brought to its final mass, nearly symmetrizing the halo in the disk plane. The effects on the halo shape do not weaken as the final disk mass is reduced by a factor of three. The axial ratios are shown for a particular equipotential surface, chosen to be about 5 kpc from the center of the disk.

The less massive disks also reorient themselves during the simulations. All four AMinor disks have similar reorientation histories, showing at most a 12 degree offset between the disk orientations. The alternate CMinor runs, however, have more divergent reorientation histories. The angle between the original CMinor disk normal and the disk normal in the alternate CMinor runs is typically around 30 degrees, rising to as high as 60-80 degrees temporarily near  $z \sim 0.7$ .

Our simulations that include gas show drastically reduced signatures of bars, and the associated heating. This reduction matches the observed decrease in the likelihood of hosting a bar in galaxies with increasing gas fraction (Masters et al. 2012). The strong effect of this massive gas component is expected because the gas offers support against self-gravity via its pressure. The extra support provided in these simulations is likely an overestimate, as realistic gas cools and forms stars, but the ability of a simple gas model

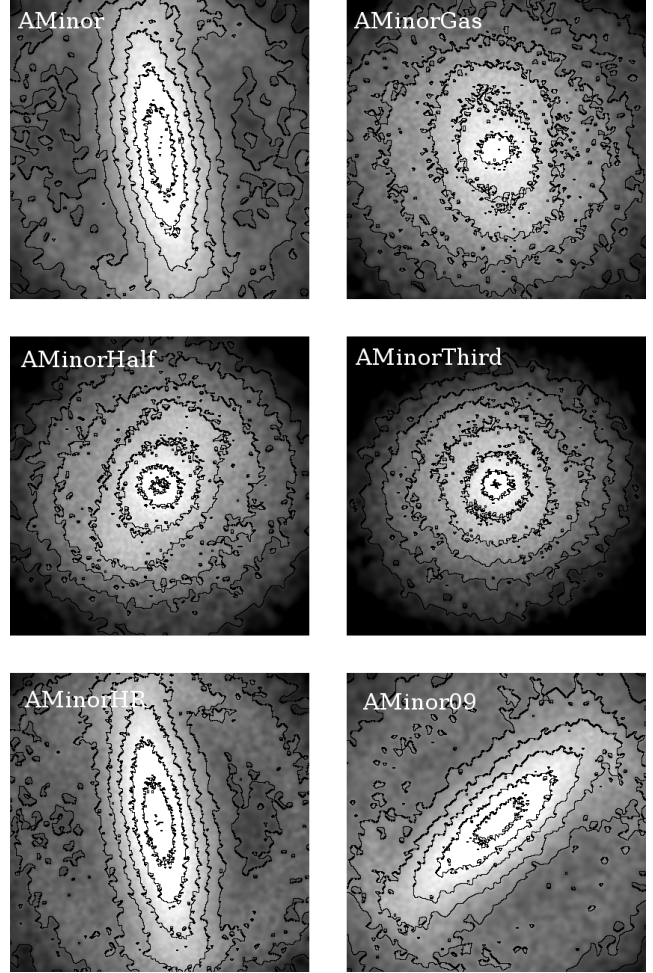


**Figure 12.** Surface density of the stellar disk at  $z = 0$ , viewed face-on, for six disk models in halo A. The models in the top two rows differ in the assumed disk masses and scale radii:  $5 \times 10^{10}$ ,  $3 \times 10^{10}$ ,  $2.5 \times 10^{10}$  and  $1.67 \times 10^{10} M_\odot$  for AMinor, AMinorGas, AMinorHalf, and AMinorThird, respectively. Reducing the disk mass or placing some baryons in a gas component helps stabilize the disk against bar formation. The two panels in the bottom row show the resulting disks in the higher resolution run ‘AMinorHR,’ and in run ‘AMinor09’ in which the disk becomes live at  $z = 0.9$  instead of 1.0; the results are nearly identical to run ‘AMinor.’ The images are 21 kpc on a side, and contours have been added to highlight the shape of the disks. The brightness of the image is logarithmic in the surface density, with all four images having the same scale.

to suppress the bar points to the need to include a realistic gas component. The lack of a strong bar also means that the subsequent bar buckling cannot occur and the central thickness of the disk is smaller at the end of the simulation.

All of our simulations start with a rigid disk potential at  $z = 1.3$  and transition to a live disk at  $z = 1.0$ . To test if any of our results is sensitive to the choice of  $z = 1.0$ , we have run a simulation of the AMinor halo in which the rigid disk becomes live at a later time of  $z = 0.9$  (‘AMinor09’ in Table 1). The qualitative features of this run are in good agreement with the AMinor run (Fig. 12): a bar forms and eventually develops an X-shape, the disk heats vertically,

and the disk reorients and shows signs of material out of the plane of the disk.

To assess the degree of convergence of these results with the resolution of the stellar disk, we have run a disk in the AMinor orientation with  $5 \times 10^5$  particles instead of  $2 \times 10^5$ , labeled AMinorHR in Table 1. The results of this simulation, e.g., the values of  $A_2$  and  $\zeta$ , agree to within 5% with the run at our fiducial resolution (see also Fig. 12). A similar degree of convergence is reported in the detailed study of Dubinski et al. (2009). Quantities such as the bar strength, pattern speed, and halo response to disk in their simulation with  $10^6$  dark matter particles and  $1.8 \times 10^5$  disk particles are very similar to those in runs with 10 and 100 times more particles.

## 6 SUMMARY AND DISCUSSION

We have presented the results of simulations of live stellar disks in the fully cosmological setting of the Aquarius simulations of dark matter haloes similar in mass to that of the Milky Way. Our simulations take place in two phases. We first allow the dark matter halo to respond adiabatically to a growing rigid disk potential between  $z = 1.3$  and 1.0. A live disk of stellar particles is then inserted and evolved self-consistently with the dark matter particles from  $z = 1.0$  to today. We have inserted disks in four Aquarius haloes (A, B, C, and D), with the disk normal initially aligned with the minor or major axis of the halo at  $z = 1.3$ . The main results in this paper are drawn from these eight simulations; several additional runs are also performed to test numerical convergences and to assess the impact of different disk models (Table 1).

The disks have a strong effect on the shapes of the inner haloes. The haloes are approximately prolate in the inner  $\sim 50$  kpc at  $z = 1.3$ . As a rigid disk potential is added, the inner haloes evolve to become oblate by  $z = 1.0$  (Figs. 1 and 2). This change occurs regardless of the disk orientation but it occurs for different reasons for the two orientations. When the disk normal is initially aligned with the halo’s minor axis, the two longer axes that define the disk plane become more symmetrized by  $z = 1.0$  due to the axisymmetric disk potential. The inner halo thus becomes nearly oblate. When the disk normal is initially aligned with the halo’s major axis, however, the original major axis shrinks and becomes the minor axis by  $z = 1.0$ . This also results in an oblate inner halo, where the disk normal aligns with the minor axis. Thus when the live disk simulation starts at  $z = 1.0$ , the disk normal is aligned with the halo’s minor axis in both of our “Major” and “Minor” runs.

For the live disks, we find striking variations in the evolution of their spatial and velocity structures between  $z = 1.0$  and 0. The A, B, and D disks form strong bars that thicken and heat the stellar particles in the inner  $\sim 10$  kpc, whereas the C disks are nearly bar-free and remain thin and vertically cold at  $R \lesssim 10$  kpc. Five of the bars experience buckling instabilities between  $z \sim 0.7$  and 0.5, resulting in a sudden increase in the vertical velocity dispersion  $\sigma_z$  and an accompanying dip in the amplitude  $A_2$  of the  $m = 2$  Fourier mode of the surface density (Figs. 6 and 7). These bars are not destroyed by the buckling but instead continue to grow from  $z \sim 0.5$  until the present day.

The behavior in the outer parts of the disks also varies greatly from disk to disk. Among the eight disks, the CMajor and CMinor disks show the largest amount of ring-like material out of the plane of the disk. Similar components are also clearly seen in the AMajor and DMinor disks (Fig. 3). These stars lie in warped planes at the outskirts, where the disk normal can twist by up to  $\sim 80$  degrees from the disk normal in the inner parts (Fig. 11). The stars in this subset of disks greatly increase the mean vertical height (Figs. 4 and 5) and the vertical velocity dispersion (Figs. 8 and 9) at  $R \gtrsim 10$  kpc, relative to the plane of the inner disk.

We have found a strong correlation between the severity of the outer warps and the amount of tumbling that the disk-halo system has undergone during the course of the simulation, i.e., the more tumbling, the larger the warps (Figs. 10 and 11). In addition, the halo and the disk are very well aligned and appear to tumble together. These trends suggest that the haloes undergoing larger tumbling experience larger tidal fields that torque the fragile outer parts of the disks.

Reducing the disk mass helps stabilize the disk against bar formation. The strong bar in the fiducial run for halo A is mostly absent when the disk mass is lowered from  $5 \times 10^{10} M_\odot$  to  $2.5 \times 10^{10} M_\odot$  and  $1.67 \times 10^{10} M_\odot$  (Figs. 12 and 13). Placing 40% of the original disk mass into a coaligned gas disk also reduced the bar drastically. The gas was not allowed to cool or form stars, thus artificially enhancing its stabilising effect. The purely stellar disk and the disks with an initial gaseous component can be thought of as bracketing the results for a more realistic gas model.

The disks presented in our simulations share many features with observed disk galaxies, although a detailed comparison would require a larger statistical sample as well as the inclusion of gas in the simulations. We can nonetheless make some broad comparisons within the limited statistics. Six of the eight disks in our simulations easily form bars at  $z \sim 0.7$  to 0.5 and the bars remain stable until the present-day. Similarly, as many as 2/3 of the nearby disk galaxies have been observed to host a bar (Marinova & Jogee 2007 and references therein). Though the evolution of the bar fraction with redshift is still a subject of ongoing debate (e.g., Jogee et al. 2004; Sheth et al. 2008), the fraction of barred disks is non-negligible out to  $z \sim 1$ . Our simulations that include gas show significantly reduced signatures of bars. This reduction matches the observed decrease in the likelihood of hosting a bar in galaxies with increasing gas fraction (Masters et al. 2012).

In addition to the prevalence of bars, as discussed in Sec 4.1, the X-shaped structures or peanut-shaped bulges that have been seen in many nearby edge-on spiral galaxies are also produced in our simulated disks (Fig. 3). One conspicuous feature in a subset of our disks is the misalignment between the orientation of the inner and outer regions of the disk (Fig. 11). By eye, the structures resemble observed warps in disk galaxies. These are quite common in the local universe, as seen in the stellar light and (particularly) in neutral hydrogen in both our own Galaxy and in other nearby systems (e.g., Kerr et al. 1957; Sancisi 1976; Reshetnikov & Combes 1998; García-Ruiz et al. 2002; Levine et al. 2006; van der Kruit & Freeman 2011 and references therein).

The circular velocity profiles,  $V_{\text{circ}}(r) = \sqrt{GM(r)/r}$ , of disks A, C, and D have broad peaks reaching 220 to 260 km/s



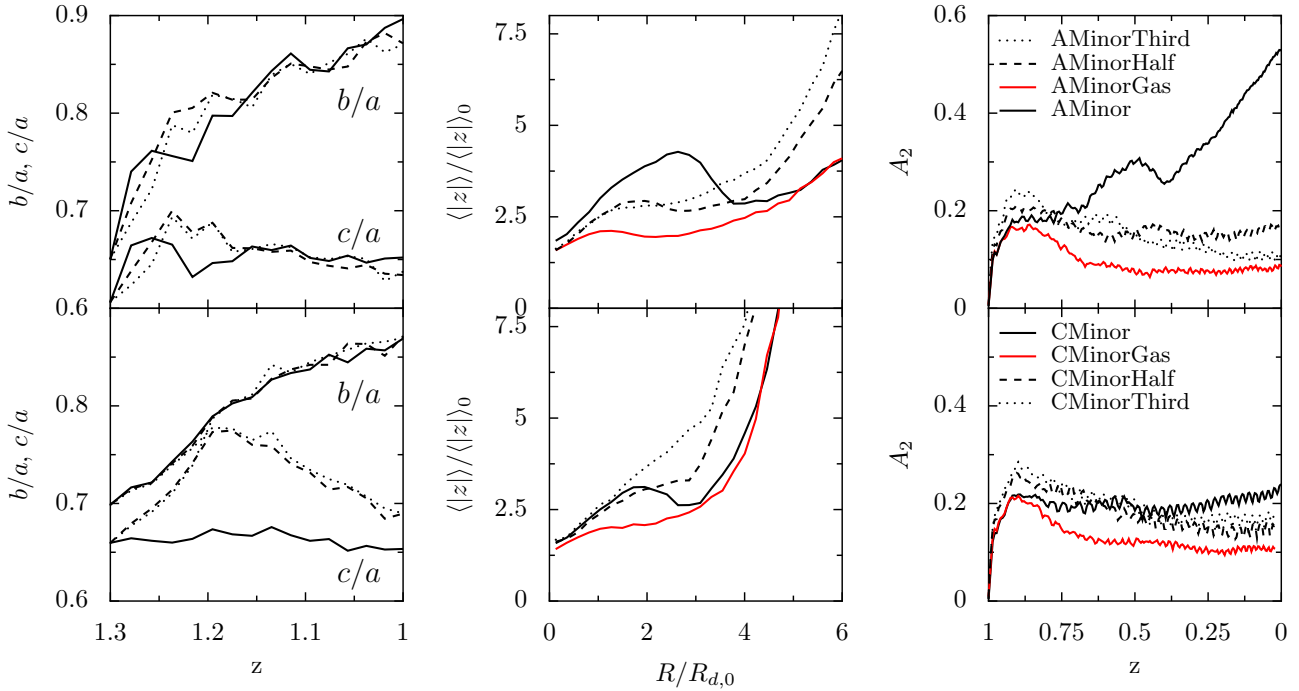


**Figure 13.** Comparison of four disk models for halo A (top row) and halo C (bottom row). The four models differ in the assumed disk mass:  $5 \times 10^{10}$ ,  $3 \times 10^{10}$ ,  $2.5 \times 10^{10}$  and  $1.67 \times 10^{10} M_{\odot}$  for runs labeled Minor, MinorGas, MinorHalf, and MinorThird, respectively. *Left:* The axial ratios of the dark matter haloes between  $z = 1.3$  and  $1.0$  hardly depend on the disk mass. *Middle:* Mean vertical distance  $|z|$  of the stellar particles from the disk plane as a function of disk radius at  $z = 0$ . Among these runs, only the AMinor and CMinor disks (black solid curves) form stellar bars, which produce a bump in  $|z|$  at a radius of  $\sim 2 - 3 R_d$ . *Right:* Bar strengths measured by the  $m = 2$  mode amplitude  $A_2$  as a function of redshift. Reducing the disk mass stabilizes the disk against bar formation. Note that the runs including gas are not included in the left panels because before the disk goes live, their evolution is identical to the original ‘Minor’ runs.

at radii between 5 and 10 kpc and decline gently outward. This is similar to the observed profile for the Milky Way (Xue et al. 2008). The virial mass of halo B is lower than that of A, C, and D by nearly a factor of two and therefore has a lower  $V_{\text{circ}}(r)$ . For the velocity dispersions, the general trend of  $\sigma_R > \sigma_{\phi} > \sigma_z$  in the inner  $\sim 10$  kpc is consistent with the Milky Way. At 8 kpc, the coldest disk (CMajor) has  $(\sigma_R, \sigma_{\phi}, \sigma_z) \approx (45, 40, 35)$  km/s at  $z = 0$ , somewhat higher than  $(38, 26, 19)$  km/s found for red stars in the solar neighbourhood (Aumer & Binney 2009). While some disks experience noticeable heating, the vertical structure of the CMajor disk stays quite constant within  $\sim 10$  kpc between  $z = 1.0$  and  $0.0$  (Fig. 5), similar to a sample of edge-on disk galaxies surveyed by Spitzer (Comerón et al. 2011).

The focus of this paper is on the gravitational interactions between live stellar disks and their host dark matter haloes in realistic cosmological simulations. We have intentionally left out discussions of the dark matter subhaloes, which are well resolved in zoom-in simulations such as the Aquarius haloes. As discussed in Sec. 4, infalling satellite galaxies, dark matter substructures, and cold gas clumps have been shown in prior studies to increase disk thickness, induce bar formation, and cause disturbances in the outer disks such as warps. On the other hand, strong bars and severe warps arise in different disks in our simulations and do not appear to be directly related. Moreover, we have demonstrated that the bar strengths depend sensitively on the disk-to-halo mass ratio, and that the outer warps are strongly correlated with the overall rotation of the disk-halo

system. Therefore, it is presently unclear if dark matter subhaloes play a major role in producing any of the disk features reported in this paper. The disks can in turn alter the fate of massive subhaloes that pass through them (e.g., D’Onghia et al. 2010). The magnitudes of all these effects depend sensitively on the orbits, masses, and concentrations of the subhaloes, in particular, on whether a massive subhalo can survive in the vicinity of the disk. We plan to quantify the impact of subhaloes on the spatial and kinematical structures of the disks and the influence of the disks on the survivability of the subhaloes in a future work.

## ACKNOWLEDGMENTS

We thank Michael Aumer, Chris McKee and Michael Boylan-Kolchin for useful discussions and suggestions, and Onsi Fakhouri for contributions to the earliest part of this project. Support for C.-P.M is provided in part by NASA through grant NNX11AI97G and grant HST-AR-12140.01-A from the Space Telescope Science Institute, and by the Miller Institute for Basic Research in Science, University of California, Berkeley. This research used resources of the National Energy Research Scientific Computing Center, which is supported by the Office of Science of the U.S. Department of Energy under Contract No. DE-AC02-05CH11231, and the Henyey cluster at UC Berkeley supported by NSF AST grant 0905801.

## REFERENCES

- Abadi M. G., Navarro J. F., Fardal M., Babul A., Steinmetz M., 2010, *MNRAS*, 407, 435
- Agertz O., Teyssier R., Moore B., 2011, *MNRAS*, 410, 1391
- Allgood B., Flores R. A., Primack J. R., Kravtsov A. V., Wechsler R. H., Faltenbacher A., Bullock J. S., 2006, *MNRAS*, 367, 1781
- Athanassoula E., 2002, *ApJ*, 569, L83
- Athanassoula E., 2008, *MNRAS*, 390, L69
- Aumer M., Binney J. J., 2009, *MNRAS*, 397, 1286
- Aumer M., White S. D. M., 2012, *ArXiv e-prints*
- Bailin J., Steinmetz M., 2005, *ApJ*, 627, 647
- Bailin J. et al., 2005, *ApJ*, 627, L17
- Benson A. J., Lacey C. G., Frenk C. S., Baugh C. M., Cole S., 2004, *MNRAS*, 351, 1215
- Berentzen I., Shlosman I., 2006, *ApJ*, 648, 807
- Berentzen I., Shlosman I., Jogee S., 2006, *ApJ*, 637, 582
- Bett P., Eke V., Frenk C. S., Jenkins A., Helly J., Navarro J., 2007, *MNRAS*, 376, 215
- Bournaud F., Jog C. J., Combes F., 2007, *A&A*, 476, 1179
- Boylan-Kolchin M., Springel V., White S. D. M., Jenkins A., Lemson G., 2009, *MNRAS*, 398, 1150
- Bureau M., Aronica G., Athanassoula E., Dettmar R.-J., Bosma A., Freeman K. C., 2006, *MNRAS*, 370, 753
- Bureau M., Freeman K. C., 1999, *AJ*, 118, 126
- Chakrabarti S., Blitz L., 2009, *MNRAS*, 399, L118
- Cole S., Lacey C., 1996, *MNRAS*, 281, 716
- Combes F., Sanders R. H., 1981, *A&A*, 96, 164
- Comerón S. et al., 2011, *ApJ*, 741, 28
- Cooper A. P. et al., 2010, *MNRAS*, 406, 744
- Curir A., Mazzei P., Murante G., 2006, *A&A*, 447, 453
- Curir A., Mazzei P., Murante G., 2007, *A&A*, 467, 509
- Curir A., Mazzei P., Murante G., 2008, *A&A*, 481, 651
- Debattista V. P., Mayer L., Carollo C. M., Moore B., Wadsley J., Quinn T., 2006, *ApJ*, 645, 209
- Debattista V. P., Moore B., Quinn T., Kazantzidis S., Maas R., Mayer L., Read J., Stadel J., 2008, *ApJ*, 681, 1076
- Debattista V. P., Sellwood J. A., 1999, *ApJ*, 513, L107
- D'Onghia E., Springel V., Hernquist L., Keres D., 2010, *ApJ*, 709, 1138
- Dubinski J., 1994, *ApJ*, 431, 617
- Dubinski J., Berentzen I., Shlosman I., 2009, *ApJ*, 697, 293
- Dubinski J., Carlberg R. G., 1991, *ApJ*, 378, 496
- Dubinski J., Chakrabarty D., 2009, *ApJ*, 703, 2068
- Efstathiou G., Lake G., Negroponte J., 1982, *MNRAS*, 199, 1069
- Font A. S., Navarro J. F., Stadel J., Quinn T., 2001, *ApJ*, 563, L1
- Frenk C. S., White S. D. M., Davis M., Efstathiou G., 1988, *ApJ*, 327, 507
- García-Ruiz I., Sancisi R., Kuijken K., 2002, *A&A*, 394, 769
- Gauthier J.-R., Dubinski J., Widrow L. M., 2006, *ApJ*, 653, 1180
- Governato F. et al., 2010, *Nature*, 463, 203
- Guedes J., Callegari S., Madau P., Mayer L., 2011, *ApJ*, 742, 76
- Hayashi E., Navarro J. F., Springel V., 2007, *MNRAS*, 377, 50
- Hopkins P. F., Hernquist L., Cox T. J., Younger J. D., Besla G., 2008, *ApJ*, 688, 757
- Jiang I.-G., Binney J., 1999, *MNRAS*, 303, L7
- Jing Y. P., Suto Y., 2002, *ApJ*, 574, 538
- Jogee S. et al., 2004, *ApJ*, 615, L105
- Jurić M. et al., 2008, *ApJ*, 673, 864
- Kazantzidis S., Abadi M. G., Navarro J. F., 2010, *ApJ*, 720, L62
- Kazantzidis S., Bullock J. S., Zentner A. R., Kravtsov A. V., Moustakas L. A., 2008, *ApJ*, 688, 254
- Kazantzidis S., Zentner A. R., Kravtsov A. V., Bullock J. S., Debattista V. P., 2009, *ApJ*, 700, 1896
- Kerr F. J., Hindman J. V., Carpenter M. S., 1957, *Nature*, 180, 677
- Kuijken K., Merrifield M. R., 1995, *ApJ*, 443, L13
- Levine E. S., Blitz L., Heiles C., 2006, *ApJ*, 643, 881
- Machado R. E. G., Athanassoula E., 2010, *MNRAS*, 406, 2386
- Marinova I., Jogee S., 2007, *ApJ*, 659, 1176
- Masters K. L. et al., 2012, *MNRAS*, p. 3344
- McMillan P. J., 2011, *MNRAS*, 414, 2446
- Mihos J. C., Walker I. R., Hernquist L., Mendes de Oliveira C., Bolte M., 1995, *ApJ*, 447, L87
- Moore B. P., Macciò A. V., Somerville R. S., Naab T., Cox T. J., 2012, *MNRAS*, 423, 2045
- Ostriker E. C., Binney J. J., 1989, *MNRAS*, 237, 785
- Purcell C. W., Kazantzidis S., Bullock J. S., 2009, *ApJ*, 694, L98
- Quinn P. J., Goodman J., 1986, *ApJ*, 309, 472
- Quinn P. J., Hernquist L., Fullagar D. P., 1993, *ApJ*, 403, 74
- Raha N., Sellwood J. A., James R. A., Kahn F. D., 1991, *Nature*, 352, 411
- Read J. I., Lake G., Agertz O., Debattista V. P., 2008, *MNRAS*, 389, 1041
- Reshetnikov V., Combes F., 1998, *A&A*, 337, 9
- Roškar R., Debattista V. P., Brooks A. M., Quinn T. R., Brook C. B., Governato F., Dalcanton J. J., Wadsley J., 2010, *MNRAS*, 408, 783
- Sancisi R., 1976, *A&A*, 53, 159
- Scannapieco C. et al., 2012, *MNRAS*, p. 2970
- Scannapieco C., White S. D. M., Springel V., Tissera P. B., 2009, *MNRAS*, 396, 696
- Sellwood J. A., Nelson R. W., Tremaine S., 1998, *ApJ*, 506, 590
- Shen S., Mo H. J., White S. D. M., Blanton M. R., Kauffmann G., Voges W., Brinkmann J., Csabai I., 2003, *MNRAS*, 343, 978
- Sheth K. et al., 2008, *ApJ*, 675, 1141
- Springel V., 2005, *MNRAS*, 364, 1105
- Springel V. et al., 2008, *MNRAS*, 391, 1685
- Tissera P. B., White S. D. M., Pedrosa S., Scannapieco C., 2010, *MNRAS*, 406, 922
- Trujillo I. et al., 2006, *ApJ*, 650, 18
- Valluri M., Debattista V. P., Quinn T., Moore B., 2010, *MNRAS*, 403, 525
- van der Kruit P. C., Freeman K. C., 2011, *ARA&A*, 49, 301
- Velazquez H., White S. D. M., 1999, *MNRAS*, 304, 254
- Vera-Ciro C. A., Sales L. V., Helmi A., Frenk C. S., Navarro J. F., Springel V., Vogelsberger M., White S. D. M., 2011, *MNRAS*, 416, 1377
- Villa-Vargas J., Shlosman I., Heller C., 2009, *ApJ*, 707, 218

- Walker I. R., Mihos J. C., Hernquist L., 1996, ApJ, 460,  
121  
Warren M. S., Quinn P. J., Salmon J. K., Zurek W. H.,  
1992, ApJ, 399, 405  
Weinberg M. D., Blitz L., 2006, ApJ, 641, L33  
Whitmore B. C., Bell M., 1988, ApJ, 324, 741  
Xue X. X. et al., 2008, ApJ, 684, 1143